Cancer associated fibroblast subtypes modulate the tumor-immune microenvironment and are associated with skin cancer malignancy

Agnes Forsthuber[1,*], Bertram Aschenbrenner[1,*], Ana Korosec[1,*], Tina Jacob[2] , Karl Annusver[2], Natalia Krajic[1], Daria Kholodniuk[1], Sophie Frech[1], Shaohua Zhu[1], Kim Purkhauser[1], Katharina Lipp[1], Franziska Werner[3], Vy Nguyen[3], Johannes Griss[3], Wolfgang Bauer[3], Ana Soler Cardona[3], Benedikt Weber[1], Wolfgang Weninger[3], Bernhard Gesslbauer[4], Clement Staud[4], Jakob Nedomansky[4], Christine Radtke[4], Stephan N. Wagner[3], Peter Petzelbauer[1], Maria Kasper[2,#] and Beate M. Lichtenberger[1,#]

Affiliations:

[1]Skin and Endothelium Research Division, Department of Dermatology, Medical University of Vienna, Austria

[2]Department of Cell and Molecular Biology, Karolinska Institutet, Sweden

[3]Department of Dermatology, Medical University of Vienna, Austria

[4]Department of Plastic, Reconstructive and Aesthetic Surgery, Medical University of Vienna Austria

* These authors contributed equally

# These authors jointly supervised this work

Corresponding authors:

beate.lichtenberger@meduniwien.ac.at

maria.kasper@ki.se

Summary

Cancer-associated fibroblasts (CAFs) play a key role in cancer progression and treatment outcome. This study dissects the yet unresolved intra-tumoral variety of CAFs in three skin cancer types — Basal Cell Carcinoma, Squamous Cell Carcinoma, and Melanoma — at molecular and spatial single-cell resolution. By integral analysis of the fibroblasts with the tumor microenvironment, including epithelial, mesenchymal, and immune cells, we characterize three distinct CAF subtypes: myofibroblast-like RGS5+ CAFs, matrix CAFs (mCAFs), and immunomodulatory CAFs (iCAFs). Notably, large cohort tissue analysis reveals marked shifts in CAF subtype patterns with increasing malignancy. Two CAF types exhibit immunomodulatory capabilities via distinct mechanisms. mCAFs synthesize extracellular matrix and have the ability to ensheath tumor nests, potentially limiting T cell invasion in low-grade tumors. In contrast, iCAFs are enriched in late-stage tumors, especially infiltrative BCC and high-grade melanoma, and express unexpectedly high mRNA and protein levels of cytokines and chemokines, pointing to their integral role in immune cell recruitment and activation. This finding is further supported by our observation that in vitro exposure of primary healthy fibroblasts to skin cancer cell secretomes induces an iCAF-like phenotype with immunomodulatory functions. Thus, targeting CAF variants, particularly the immunomodulatory iCAF subtype, holds promise for improved efficacy of immunotherapy in skin cancers.

Introduction:

Fibroblasts have been considered as rather simple structural cells, which largely contribute to extracellular matrix deposition in connective tissues and tissue repair, for a long time. However, they present with an unprecedented plasticity and functional heterogeneity especially in pathological conditions, and exert a significant influence on different cells in their microenvironment, thus, modulating different processes. In cancer, fibroblasts have been established as a key component of the tumor microenvironment (TME) affecting both cancer progression and the response to therapies. Fibroblast heterogeneity has been acknowledged previously as playing both tumor suppressive as well as tumor supportive roles [1–7]. Recent studies even demonstrated that also mutations in fibroblasts can lead to cancer[8], further highlighting their impact on tumorigenesis. It also has become clear that in a single tumor several fibroblast subtypes exist in parallel with different functions [9]. Single-cell RNA sequencing (scRNA-seq) has revealed manifold dermal fibroblast subpopulations in mouse and human healthy skin [10–12]. Likewise, fibroblast heterogeneity has been studied in many cancers such as breast cancer [13,14], pancreatic ductal adeno carcinoma [15,16], colorectal cancer [17,18], head and neck squamous cell carcinoma [19] and many more [20]. Comparable single-cell transcriptomics studies in skin cancer are missing. The few previous scRNA-seq based studies of human melanoma, basal cell carcinoma (BCC) and cutaneous squamous cell carcinoma (SCC) mainly focused on tumor infiltrating lymphocytes, thus these datasets included only a few or no fibroblasts (Supplemental Table 1) [21–27]. In the past years, scRNA-seq revealed a range of different cancer-associated fibroblast (CAF) subsets with newly described markers in

various tissues. Besides context-dependent and/or uniquely described CAF subsets in certain types of cancer [28–30], a common trait among many of these studies is the presence of a CAF subtype with immunomodulating characteristics, secreting IL6 and other proinflammatory cytokines, and a CAF subtype with a myofibroblastic phenotype defined by its widely accepted signature molecule alpha smooth muscle actin (ACTA2) [13,14,31–36].
In healthy skin, lineage tracing mouse models and functional studies in mouse and human skin identified two major fibroblast subsets, the papillary fibroblasts in the upper dermis and the reticular fibroblasts of the lower dermis. They exhibit distinct roles during skin development, wound healing and fibrotic skin disorders, [37–40]. Whether these two subpopulations evolve into CAFs, or impact skin tumor progression differently, is still an unresolved topic. So far, all studies on skin CAFs focused on CAFs as a unit, their overall marker gene expression, capability to stimulate migration of tumor cells, secretion of soluble mediators, and their response to anti-tumor therapies [41–43], leaving a major gap in knowledge about the presence of CAF subtypes, their association with tumor malignancy and different functional roles, which we address in this study.

Here, we investigated the cellular ecosystem of BCC, SCC and melanoma – with emphasis on fibroblast heterogeneity – using the sensitive Smart-seq2 scRNA-seq platform (n=10 tumors) and mRNA staining *in situ* (n=68 tumors). SCCs vary from well to poorly differentiated with increasing metastatic potential [44,45], and BCCs, which metastasize very rarely, are primarily tissue-destructive locally [46,47]. Both cancer types arise from keratinocytes. In contrast, melanoma is a skin cancer type derived from melanocytes that comes with a high potential of metastatic spread and poor survival rates, which have improved significantly due to novel therapeutics, especially immunotherapies [48,49]. The unique combination of these three different types of skin tumors in one dataset allowed us to dissect similarities and differences between those cancer types with a special focus on the fibroblast heterogeneity in a healthy skin, premalignant and cancer context. Collectively, our work deconstructed CAF heterogeneity in skin cancer, which led to important new insights. We show that the mCAF subtype, which forms a dense extracellular matrix network at the tumor-stroma border, likely plays a role in T cell marginalization, and propose that the iCAF subtype is an important regulator of immune cell recruitment and immune surveillance.

Results:

A collective single-cell atlas of primary BCC, SCC and melanoma to deconstruct skin cancer

To explore fibroblast heterogeneity and their cross talk to tumor and immune cells, we collected biopsies from four cutaneous squamous cell carcinomas (SCCs), three basal cell carcinomas (BCCs), three melanomas and biopsies of sun-protected skin from five healthy donors (Supplemental Table 2). For the tumor samples, fresh 4 mm punch biopsies from the tumor center and from non-lesional adjacent skin (providing sex- and age-matched healthy skin controls) were collected directly after surgery. Since previous single cell transcriptomic

83 studies of skin cancer included no fibroblasts or only low CAF numbers (Supplemental Table
84 1), instead of random droplet-based sampling of tumor-associated cells, we chose a FACS-
85 sorting approach to enrich for fibroblasts and to gain highly sensitive scRNA-seq data using
86 Smart-seq2 technology. Upon dissociation of the tissues, the samples were enriched for
87 keratinocytes, fibroblasts and immune cells by FACS (Figure S1A and S1B) and the cells were
88 directly sorted into 384-well plates for sequencing with the Smart-seq2 technology (Figure
89 1A). In two healthy control samples a random live-cell sorting approach was used, explaining
90 why keratinocytes are underrepresented in these samples (Healthy I, Healthy II, Figure 2A),
91 which was compensated by a separate keratinocyte enrichment protocol in healthy samples
92 Healthy III-V (Figure S1A and 2A). In total, 5760 cells were sequenced, finally retaining 4824
93 cells at a median depth of 486146 RPKM/cell and a median of 3242 genes/cell after quality
94 control and filtering (Figure S1C). Cell numbers per sample after quality filtering are shown in
95 Figure S1D. Unsupervised clustering separated cells into fibroblasts, healthy and malignant
96 keratinocytes as well as melanocytes, immune cells, and endothelial cells (Figure 1B).
97 Assignment of cell type identity was based on commonly accepted signature gene expression:
98 *COL1A1* and *PDGFRA* for fibroblasts, *RERGL* for vascular smooth muscle cells (vSMC), *KRT5*,
99 *KRT14* and *CDH1 (E-cadherin)* for keratinocytes, *CD45* for immune cells, *TYR*, *MITF* and *MLANA*
100 for melanocytic cells and *CDH5* for endothelial cells (Figure 1B and 1C).
101
102 **Tumor cells express a range of additional keratins**
103 Second-level clustering of healthy and neoplastic keratinocytes resulted in a clearly separated
104 cluster of healthy keratinocytes (hKC) with basal (*KRT5*, *KRT14*, *COL17A1*) and
105 differentiating/suprabasal (*KRT1*, *KRT10*) marker gene expression. The majority of cells in
106 clusters KC1–KC5 contained tumor cells from BCC and SCC samples, with tumor cells
107 expressing a range of additional keratins that are not expressed by healthy skin keratinocytes
108 (Figure 2A and Supplementary table 2). For example, BCC cells expressed *KRT5*, *KRT14* and
109 additionally *KRT17* [50], which are foremost clustering in KC2 and KC3. As expected for the
110 Hedgehog(Hh)-pathway-dependent BCC, we confirmed *PTCH1/2* as well as *GLI1/2*
111 overexpression in clusters KC2 and KC3 (Figure 2A, S2A and S2B) [51]. Cells from the SCC samples
112 clustered in KC1, KC2, KC4 and KC5. KC1 – which primarily comprised cells of donor sample
113 SCC III (Figure 2A and S2C) – expressed in addition to *KRT5*, *KRT14*, and *KRT17* the typical SCC
114 keratins like *KRT6A* and *KRT16,* and showed reduced expression of *KRT1* and *KRT10* [50] (Figure
115 2A). Cells from donor sample SCC IV, a SCC arisen from Bowen's disease (Supplemental Table
116 2), mainly clustered in KC2, KC4, and KC5 that showed reduced expression of *KRT1*, *KRT10*.
117 KC2 and KC5 also displayed expression of *KRT16* and *KRT19,* respectively, which has been
118 previously described for this SCC subtype [50] (Figure 2A and S2C). Notably, *KRT7*, *KRT18* and
119 *KRT19* were only expressed by KC1 and KC5, which were primarily represented by cells
120 originating from SCC samples (Figure 2A and S2C). It has been shown that tumors co-opt
121 developmental programs for their progression [1]. In our dataset we find previously described
122 keratins of the simple skin epithelium of the first trimester embryo such as KRT18 and KRT19
123 expressed in SCC cluster KC1 and KC5, or *KRT8* expressed in BCC cluster KC2 [52] (Figure 2A).

124 Interestingly, also healthy keratinocytes contributed with more than 25% to KC5, which likely
125 represent luminal cells from sebaceous or sweat glands expressing the marker genes *KRT7*,
126 *KRT19*, *SFRP1* and *DCD* [53]. In KC4, keratinocytes from BCC, SCC, melanoma as well as healthy
127 skin clustered together. These cells did not express unified classical keratinocyte markers
128 (Figure 2A) but presented with a scattered expression of different hair follicle-associated
129 keratins (data not shown). This expression pattern suggests that KC4 contains keratinocytes
130 of the different anatomical structures of the hair follicle in line with KC4 cluster's position next
131 to the BCC keratinocytes (KC3) and the presence of *PTCH1/2* and *GLI1/2* expressing cells
132 (Figure 2C and Figure S2 A-B).
133
134 **The tumor microenvironment strongly impacts non-malignant cell types**
135 Second-level clustering of melanocytes and melanoma cells revealed one cluster of healthy
136 melanocytes (hMC) derived from healthy skin samples, and one separate cluster of non-
137 malignant melanocytes derived mainly from SCC and BCC samples (tumor melanocytes, tMC).
138 This separate clustering can likely be explained by the influence of the TME on the expression
139 pattern of melanocytes in comparison to melanocytes from healthy skin. The melanoma
140 samples separated into four different donor-specific clusters: MEL1 and MEL2 coming from
141 Melanoma I, MEL3 from Melanoma II, and MEL4 from Melanoma III (Figure 2B and
142 Supplementary table 2). In order to explain this donor-specific clustering, as well as to
143 segregate malignant from non-malignant cells, we inferred copy number variation (CNV)
144 analysis on our scRNA-seq data using the R package *inferCNV* [19,25]. We performed CNV analysis
145 for melanocytes and melanoma cells, and a separate CNV analysis for healthy and malignant
146 keratinocytes, as previously described [19], using healthy stromal cells (fibroblasts, vascular
147 smooth muscle cells and pericytes) as a reference (Figure 2C and S3). Melanoma cells, which
148 are known for their high mutational load [54], displayed strong CNV patterns. Remarkably, these
149 patterns were donor-specific despite of sharing the same histological subtype
150 (acral lentiginous melanoma, ALM) and body location (heel/toe) (Supplementary table 1).
151 Among BCC and SCC samples, SCC III (forming cluster KC1) presented with the strongest CNV
152 pattern, which matched well with its histopathological characterization of a poorly
153 differentiated, aggressive type of SCC (Supplementary table 2). In addition to the CNV
154 analysis, we also utilized high *PTCH1* and *PTCH2* expression[55,56] (*PTCH1/2 high)* in comparison
155 to the healthy skin cluster hKC to pinpoint tumor cells (Figure 2A and S2A,B). As the non-
156 malignant cells mixed across almost all donor samples, such as tMC or immune cells (Figure
157 2B-D), we did not regress for donor differences; thus, donor-specific tumor cell clustering in
158 KC1 and MEL1–MEL4 is likely the result of genomic aberrations and not an effect of batch
159 variations.
160
161 Subclustering of immune cells resulted in eight immune cell clusters, including T and B cells,
162 granulocytes and antigen presenting cells (Figure 2D and S2C). Interestingly, CD4 and CD8 T
163 cells from healthy samples (hTcells) formed a distinct cluster, adjacent to CD4 (tCD4) and CD8
164 T cells (tCD8) from tumor samples (Figure 2D and S2C). This can be explained by a different

activation status of T cells in healthy or tumor samples: Increased expression of granzymes, perforin and *IFNγ* indicated T cell activation in CD8 T cells from tumor samples versus healthy tissue (Figure 2E). Regulatory T cells (Tregs), *CD4*$^+$*IL2RA*$^+$*FOXP3*$^+$, were found mixed with CD4 T cells from tumor samples (tCD4) (Figure 2D, 2E and S2C).

Fibroblasts from healthy skin cluster separately from CAFs

Second-level clustering of fibroblasts and vSMCs (2239 cells) resulted in 7 subclusters: two main clusters from healthy skin samples (papillary fibroblasts (pFIB), reticular fibroblasts (rFIB)), four CAF subclusters (matrix CAFs (mCAF), immunomodulatory CAFs (iCAF), *RGS5*$^+$ CAFs and pericytes (*RGS5*$^+$ cells), unclassifiable CAFs (ucCAF)), and one vSMC cluster (Figure 3A, S4A and S4B). We used differentially expressed genes as well as commonly accepted markers to define these subclusters. Reassuringly, fibroblasts from the tumor-adjacent skin samples were found on the transition between healthy and tumor samples, and within the *RGS5*$^+$ as well as vSMC cluster (Figure S4A), indicating that CAFs may develop from skin-resident fibroblasts (pointing towards field cancerization) [57].

Importantly, several established markers for papillary and reticular fibroblasts could be assigned to the two subclusters comprising cells from healthy donors. *COL6A5*, *COL23A1* and *HSPB3* [10], the Wnt inhibitors *APCDD1* and *WIF1* [10,58], *NTN1* and *PDPN* [59] are commonly accepted markers for papillary fibroblasts and were found to be expressed in the pFIB cluster. *DPP4* (*CD26*), which was described as a marker for papillary fibroblasts by Tabib et al. 2018, was expressed in both subpopulations in our data (Figure S4C), as shown by Korosec et al., 2019 and Vorstandlechner et al., 2020 [12,39]. The healthy fibroblast subcluster rFIB expressed genes that are characteristic for reticular fibroblasts: *THY1* [39], *FMO1*, *MYOC* and *LSP1* [11], *MGP* and *ACTA2* [59] as well as the preadipocyte marker genes *PPARG* and *CD36* [39] (Figure S3C). However, we could not confirm the expression of various other published reticular fibroblast markers. The discrepancy of marker expression in distinct datasets might result from tissue collection from different body sites, tissue preparation or sequencing technology. Furthermore, several markers were identified in *in vitro* cultures, mostly on protein level. Thus, we conclude that the healthy fibroblast cluster pFIB represents papillary fibroblasts, and rFIB represents reticular fibroblasts (Figure 3A, 3B and S4C).

Different skin cancer types comprise both common and tumor type-specific CAF subsets

Subclustering segregated four CAF populations: mCAFs, iCAFs, *RGS5*$^+$ cells, and ucCAFs. Matrix CAFs (mCAFs) exhibited increased expression of extracellular matrix components such as collagens (*COL1A1*, *COL1A2*, *COL3A1)*, Lumican (*LUM*), Periostin (*POSTN*) or Tenascin-C (*TNC*) compared to all other fibroblast clusters (Figure 3A and 3B). Immunomodulatory CAFs (iCAFs) presented with enhanced expression of the matrix remodelers *MMP1* and *MMP3*, the pro-inflammatory cytokines *IL6* and *CXCL8* and the immune-suppressive molecule *IDO1* among their top ten differentially expressed genes (DEGs), thus suggesting an immunoregulatory and cancer invasion-supportive phenotype (Figure 3A and 3B). Intriguingly, the mCAF cluster

206 harbored fibroblasts from all BCC and well-differentiated SCC samples (mainly SCC I and SCC
207 IV), whereas the iCAF cluster contained fibroblasts from all melanoma samples, one poorly
208 differentiated SCC (SCC III) and one BCC (BCC II). While the presence of these subsets seems
209 to depend on the skin cancer type with iCAFs being associated with the most aggressive
210 tumors, *RGS5*$^{+}$ cells were found in all tumor samples independently of skin cancer type and
211 malignancy (Figure 3A, S4A and S4B). Notably, mCAFs and iCAFs expressed different
212 transcription factors (TFs; Figure 3C). In mCAFs, TFs associated with conserved developmental
213 proteins, including genes of the WNT pathway (*CXXC5*, *TCF4*), transcriptional regulation of
214 mesenchymal cell lineages (*TWIST1*, *TWIST2*), and anti-inflammatory signaling (*KCNIP3*), were
215 upregulated. iCAFs expressed high levels of TFs that are related to immune responses such as
216 *STAT1*, *IRF1*, *IRF9* or *ARID5A*. Of note, there is also a difference in TF expression between SCC-
217 and melanoma-derived iCAFs.
218
219 Since *RGS5*$^{+}$ cells express *ACTA2* (in combination with *COL1A1*, Figure 4A), this subset likely
220 represents activated fibroblasts that are usually termed myofibroblasts in wounded or fibrotic
221 tissues [60], or myoCAFs in different cancer types [35]. However, they also express genes among
222 their top DEGs that have been used as pericyte markers, such as *RGS5*, *KCNJ8, ACTA2* and
223 *MCAM* (Figure 3B) [61–63]. *RGS5*$^{+}$ cells also share some markers with the vSMC cluster, such as
224 *ACTA2*, *TAGLN* and *MCAM*, which are markers for perivascular cells in various tissues [39,64]. The
225 vSMC population formed its separate cluster and was clearly defined by *RERGL*, *MYH11*, *CNN1*
226 in addition to *ACTA2* [62] (Figure 3A and 3B). Unclassifiable CAFs (ucCAFs) represent a minor
227 population with an inconclusive gene expression pattern and mixed cell contribution from
228 almost all tumor samples, which we therefore did not consider further for in-depth discussion
229 (Figure 3A and 3B).
230
231 **Trajectory inference shows two main differentiation routes for CAFs from healthy cells**
232 Trajectory analysis using Monocle2 and Monocle3 [65,66] showed that healthy fibroblasts follow
233 two differentiation routes: either towards mCAF/iCAF or towards *RGS5*$^{+}$cells (Figure 3D and
234 3E). Note that the vSMC cluster was excluded from trajectory inference as we do not expect
235 them to differentiate from healthy fibroblasts and CAFs from a biological point of view. The
236 trajectory analysis also shows that iCAFs are a differentiation endpoint, with mCAFs being an
237 intermediate state, and thus it may be possible that iCAFs develop from mCAFs. This might
238 also be supported by the fact that iCAFs express several mCAF genes albeit at a lower level,
239 while mCAFs do not express iCAF markers (Figure S8A and S8B). Fibroblasts from tumor
240 adjacent skin samples are preferentially found in the healthy fibroblast and the RGS5^{+} cells
241 branches, and a smaller fraction bridging to the mCAF branch, indicating that they are in a
242 transitory position between healthy fibroblasts and CAFs.
243
244 ***ACTA2* and *FAP* in combination identify all CAF subpopulations in skin tumor samples**
245 Previous studies have used different single markers like ACTA2 or FAP to identify or isolate
246 CAFs in different tissues [67]. However, a query on previously described CAF marker genes

247 showed that, in our dataset, most of them are either restricted to a distinct CAF subset, or
248 found in all fibroblast clusters including healthy fibroblasts, but do not solely identify all CAF
249 subsets (Figure S4D). A good strategy to detect all CAFs within skin tumor samples is
250 combining the two most frequently used CAF markers *ACTA2* and *FAP*. Although this
251 combination also includes vSMCs, it allows to enrich for all CAF subpopulations when used
252 together (Figure S4D).
253
254 **The *RGS5*$^{+}$ cells are best described as a mixed population of myoCAFs and pericytes**
255 When we investigated the detailed gene expression profiles of the distinct CAF subtypes we
256 suspected that the *RGS5*$^{+}$ cluster likely comprises both myoCAFs and pericytes, therefore we
257 chose the neutral term "*RGS5*$^{+}$ cells" for this cluster. In detail, *RGS5*$^{+}$ cells expressed *ACTA2* –
258 the signature gene for myofibroblasts and myoCAFs – in combination with *COL1A1*. The
259 expression of *PDGFRB*, *TAGLN*, *RGS5*, *DES* and the absence of *PDGFRA* suggests that this
260 cluster also comprises pericytes [61–63] (Figure 4A). Interestingly, the *RGS5*$^{+}$ cluster also shows
261 expression of *NOTCH3*, *EPAS1*, *COL18A1* and *NR2F2*, markers that were used to describe so-
262 called vascular CAFs (vCAFs), a CAF subset defined by Bartoschek et al., 2018 in a mouse model
263 for breast cancer [68] (Figure S5A). Of note, endothelial markers such as *CDH5*, *PECAM1*, *TIE1*
264 or *CD62* were not expressed in the *RGS5*$^{+}$ cluster (Figure S5B).
265
266 To characterize the nature of the *RGS5*$^{+}$ cluster further, we stained tumor sections for
267 Transgelin (TAGLN), which is a prominently expressed gene in this cluster. This tissue staining
268 revealed TAGLN protein along blood vessels as expected, but also within the tumor stroma
269 without direct contact to vessel-like structures (Figure 4A). Protein expression of Desmin
270 (DES), a marker for pericytes and vSMCs [60,61] was restricted to vessels (Figure 4A). *DES* was
271 only expressed by few cells on RNA level, which was not sufficient to identify a separate
272 pericyte cluster within the *RGS5*$^{+}$ cells in our sequencing data set [69,70]. Next, we performed
273 mRNA co-staining for *RGS5, COL1A1* and *PDGFRA* mRNA to validate our sequencing data and
274 to verify the stromal and perivascular presence of *RGS5*$^{+}$ cells (Figure 4B, Figure S5C). In tumor
275 regions (Figure 4B region 1-3 and S4C region 1-2), a positive staining for *RGS5* was detected
276 both at vessel-structures and within the stroma, in comparison to the peritumoral area,
277 where *RGS5* staining was only found surrounding vessel-like structures (Figure 4B, region 4).
278
279 To shed light on the discrepant classification of cells as being myofibroblast-like CAFs or
280 pericytes in tumor samples, we reanalyzed a publicly available head and neck squamous cell
281 carcinoma (HNSCC) data set [19] and put it in comparison with our dataset. Puram et al.
282 classified the tumor fibroblasts into CAFs, myofibroblasts and intermediate (resting)
283 fibroblasts. We extended their published marker gene set by commonly accepted pericyte
284 markers and found those enriched in the myofibroblast cluster only, revealing a very similar
285 expression profile to our *RGS5*$^{+}$ cell cluster (Figure 4C). The fact that this formerly defined
286 myofibroblasts have been defined as pericytes upon reanalysis by another group [71], suggests
287 that myofibroblasts and pericytes share a very close gene expression pattern which indeed

288 does not allow segregation by transcriptional profiling. Thus, the absence of histological
289 stainings in previously published datasets impeded an accurate definition of those cells, and
290 only the combination of histological localization and gene expression allows proper lineage
291 designation. We conclude that the *RGS5*$^{+}$ cell cluster within our as well as the HNSCC dataset
292 comprises both pericytes and CAFs.
293
294 ***In situ* validation and spatial localization of mCAF and iCAF subsets**
295 We verified the presence of iCAFs and mCAFs by mRNA staining *in situ* in the same tumor
296 samples that were sequenced as well as in additional independent tumor biopsies (n=68
297 tumors in total). We used *COL11A1* and *PTGDS* as markers for mCAFs, and MMP1 (and several
298 cytokines) as a marker for iCAFs, in co-stainings with the pan-fibroblast marker *COL1A1*
299 (Figure 5A, 5B, 6C, S6 and S7). The distribution of mCAFs and iCAFs in the tumor tissue follows
300 different patterns: mCAFs were found abundantly in large patches ensheathing tumor nests,
301 but also pervading the tumor in strands (Figure 5A and S6A). Importantly, mCAFs were
302 especially enriched at the tumor-stroma border of BCC and well-differentiated SCC (Figure
303 S6A). Contrary, iCAFs were found in smaller numbers intermingled between *MMP1*$^{-}$*COL1A1*$^{+}$
304 cells intratumorally in stromal nests and strands that pervade the tumors or in patches at the
305 invasive front (Figure 5B and S6B). To verify our scRNA-seq data suggesting that iCAFs are
306 predominant in aggressive tumors, we stratified the tumor samples into different categories:
307 nodular and infiltrative BCC, well-differentiated and poorly-differentiated SCC, and low-grade
308 (Tis and ≤T1) and high-grade (≥ T3) melanomas (n=52). Large-field spatial visualization of the
309 CAF subpopulations in tumor tissue samples showed a clear change in the CAF patterns from
310 lower to higher malignancy, along with a higher overall CAF density in the aggressive variants
311 of the respective skin cancer subtypes (Figure 5C). To quantify this difference in CAF subsets,
312 the regions of interest (ROIs) were set within the tumor as well as at the invasive front (Figure
313 5C,D and S7A; see Methods). The total CAF density significantly increased in infiltrative BCC
314 compared to nodular BCC, and in high-grade melanoma compared to low-grade melanoma
315 (Figure 5D). Also the iCAFs displayed an increase in number between nodular BCC and
316 infiltrative BCC, and low grade (≤ T1) and high grade (≥ T3) melanomas, respectively (Figure
317 5D). The SCC subtypes displayed a similar iCAF trend; however, it was not statistically
318 significant (see Discussion). This extended data analysis, which also included infiltrative BCC
319 and low-grade melanoma samples, confirmed the scRNA-seq data showing that iCAFs are
320 more abundant in more malignant skin cancer subtypes, particularly in infiltrative BCC and
321 high-grade melanoma. Interestingly, also the mCAFs increased in abundance in infiltrative
322 BCC compared to nodular BCC, and high grade (≥ T3) versus low grade (≤ T1) melanomas
323 (Figure 5D, Discussion).
324
325 **mCAFs form a barrier around tumor nests**
326 We investigated the expression of matrix-associated genes (collagens, laminins, lysyloxidases
327 and other ECM genes) and immune response or cancer invasion-associated genes (MMPs,
328 chemokines, interleukins and immunomodulatory genes) by module scores and found a

329 significant enrichment of matrix-associated genes in mCAFs and immuno/invasiveness-
330 associated genes in iCAFs (Figure S8A and S8B). Additionally, we interrogated for possible
331 ligand-receptor interactions: mCAFs exhibit a strong expression of collagens and other ECM
332 genes, whose receptors are found on healthy and neoplastic keratinocytes and melanocytes
333 as well as on immune cells (Figure S9A and S9B). COL11A1 protein staining revealed a dense
334 network of collagen fibers aligning the basement membrane of tumor nests (Figure 5E),
335 indicating that mCAFs may control T cell marginalization as has been shown for COL11A1
336 expressing CAFs in lung cancer [72]. Thus, we quantified the number of mCAFs and $CD3^+$ cells in
337 the total cancer tissue (including tumor stroma) and the number of $CD3^+$ cells within tumor
338 nests of several ROIs per sample of nodular and infiltrative BCC samples (n=15, 97 ROIs). The
339 number of mCAFs/mm^2 tissue negatively correlated with $CD3^+$ cells/mm^2 within tumor nests
340 (Figure 5F), suggesting that mCAFs may form a physical barrier to inhibit T cell infiltration into
341 tumor nests. Of note, while total CAF and mCAF numbers negatively correlate with CD3
342 cells/mm^2 in tumor nests, iCAF numbers did not (Linear regression: total CAFs: R^2=0,039;
343 mCAFs: R^2=0,040; iCAFs: R^2=0,009). Indeed, representative images from overlaid CD3 and
344 mCAF stainings ($COL1A1^+COL11A1^+$) show that infiltration of $CD3^+$ cells foremost occurs at
345 areas where staining of mCAFs is low or absent (Figure 5F).
346
347 **iCAFs are the major source of cytokines in the TME and are capable of activating T cells**
348 iCAFs strongly express immunomodulatory genes, including *TGFB3* and *LGALS9*,
349 proinflammatory cytokines such as *IL1B* and *IL6* (Figure 6A and S8B). Additionally, iCAFs
350 express high levels of a plethora of chemokines in comparison to healthy or neoplastic
351 keratinocytes and melanocytes (Figure 6A upper heatmap), and thus likely regulate the
352 immune cell composition and influence immune surveillance in the tumor as their receptors
353 are found on many different immune cells. (Figure 6A and 6B). Notably, iCAFs from melanoma
354 samples express high levels of *CXCL1-8* but not *CXCL9-13*, whereas the expression of *CXCL9-*
355 *13* is high in iCAFs of the SCC III and BCC II sample. Only *CXCL2* is equally high expressed in
356 iCAFs from all tumor samples (Figure 6A). Similarly, *IL1B* is expressed at much higher levels in
357 iCAFs derived from melanoma, while *TGFB3* and *LGALS9* are strongly expressed in iCAFs from
358 BCC and SCC but not melanoma (Figure 6A). We also made a receptor-ligand interrogation
359 with CellChat and confirmed several predicted interaction partners of iCAFs and mCAFs as a
360 signaling source (Figure 6B and S9) [73]. We further confirmed the CAF-derived expression of
361 cytokines by mRNA stainings *in situ* (Figure 6C, S7B). *CXCL2*, *CXCL8* and *IL24* were selected for
362 the analysis because these three cytokines showed a good coverage across the iCAF cluster,
363 although cell- and sample-specific differences remain (Figure S7B,C). As visualized in the
364 spatial plots of representative samples, cytokine-expressing CAFs are more abundant in the
365 most aggressive tumor variants (infiltrative BCC, poorly differentiated SCCs, and high-grade
366 melanoma) (Figure S7B). While the majority of nodular BCC and low-grade melanomas
367 harbored no or single dispersed cytokine-expressing CAFs, several infiltrative BCC and high-
368 grade melanoma presented with multiple clusters of cytokine-expressing CAFs (Figure 6C),
369 which is in line with the *in situ* quantification of iCAFs (Figure 5C,D) and transcriptomic data

370 (Figure S4A). The difference in cytokine-expressing CAF density and distribution was not as
371 pronounced between well and poorly-differentiated SCCs, although they appeared to be
372 more frequent in late-stage SCC (Figure 6C and S7B). Furthermore, we confirmed that CAFs
373 are a major source for cytokines in the TME in an entirely independent single cell
374 transcriptomics dataset of melanoma (n=5) (Figure S8C). These samples express exceptionally
375 high levels of *CCL2*, *CXCL12* and *CXCL14*. Along these lines, also CAFs from oral SCCs display
376 stronger cytokine expression than their respective tumor cells (Figure S8D).
377 These results led us to hypothesize that the cancer cells of invasive cancers (but not from non-
378 invasive ones) may directly impact the phenotype of tumor-adjacent fibroblasts. To test this,
379 we isolated primary dermal fibroblasts from healthy skin (NHDF) and treated them with
380 conditioned media collected from melanoma and SCC cell lines (Figure S10A). Intriguingly, the
381 conditioned media of cultured cell lines derived from melanoma metastases (VM08 and
382 VM15 from lymph node metastasis) or from a highly aggressive SCC (SCC13) [74] strongly
383 induced the expression of different cytokines and chemokines in healthy skin fibroblasts
384 (Figure 6D). Likewise, these cytokines and chemokines were expressed at high levels by
385 fibroblasts isolated from a primary melanoma without further treatment (pMel CAFs; Figure
386 6D). On the contrary, VM19 and VM25 cell lines, which were derived from primary
387 melanomas, did not induce cytokine expression (except CXCL8 by VM25). The melanoma cell
388 line VM26 derived from a subcutaneous metastasis [75] only induced higher levels of *CCL2* but
389 not the other tested cytokines and chemokines. Although the cancer cells expressed several
390 cytokines themselves (Figure 6D), it was striking that the supernatant of these cancer cell lines
391 induced even more cytokines and chemokines in healthy fibroblasts. Importantly, we
392 confirmed the expression of several cytokines and chemokines by fibroblasts and induced
393 iCAFs on protein level with LEGENDplex assays (Figure S11).
394 Intriguingly, while the conditioned medium from cancer cells alone induced the expression of
395 iCAF-related genes (cytokines, chemokines, Figure 6D), expression of ECM-related genes was
396 not induced (Figure S10B). Thus, we conclude that the secretome of invasive tumor cell lines
397 can transform normal fibroblasts into iCAF-like, but not mCAF-like cells *in vitro*.
398 Furthermore, naïve CD4 and CD8 T cells were co-cultured together with NHDFs that were
399 pretreated with conditioned medium from VM15, VM26, VM19, VM25 or control medium,
400 and with pMEL CAFs. In parallel, naïve CD4 and CD8 T cells were co-cultured with the cancer
401 cells directly. We demonstrated that primary fibroblasts isolated from healthy skin are
402 capable of activating T cells (Figure 7A-C and S12A), as shown by increased percentages of
403 proliferating CD4 and CD8 T cells (Figure 7B) and activated CD69+ CD4 and CD8 T cells (Figure
404 7C, S12A and S12B). This potential to activate T cells was enhanced when fibroblasts were
405 exposed to the secretome of cancer cells. Comparing cancer CM-treated NHDFs to untreated
406 NHDFs, showed a further increase in CD4 T cell proliferation with CM derived from VM15 and
407 VM26, and in CD8 T cell proliferation with CM derived from VM15, VM26 and VM19. Early T
408 cell activation was promoted by VM15- and VM19-derived CM for CD4 T cells, and by VM15-
409 derived CM for CD8 T cells (Figure 7C). Late activation of CD4+ T cells measured as percentage
410 of CD45RO+/CD62L- T cells at 96h was significantly enhanced by CM derived from VM15,

411 VM26 and VM19 (Figure S12C and S12D). Importantly, also CAFs directly isolated from a
412 primary melanoma without further treatment (pMel CAFs) were potent in activating CD4 and
413 CD8 T cells (Figure 7B,C).
414
415 Taken together, *in situ* stainings of the marker genes identified in our scRNAseq screen
416 showed that mCAFs and iCAFs are distinct CAF populations that follow different distribution
417 patterns *in situ* (Figure 7D*)*. mCAFs are present in all tumors but seem to play an important
418 role at the tumor-stroma border as they form dense networks surrounding tumor nests of
419 benign tumors, i.e. nodular BCC and well differentiated SCC. In contrast, the number of iCAFs
420 increases significantly in aggressive tumors (especially infiltrative BCC and late-stage
421 melanoma) and, thus, high abundance of iCAFs correlates with malignant progression (Figure
422 5D and 7D). Importantly, receptor-ligand analysis revealed that iCAFs, which are associated
423 with late-stage tumors, express many immunomodulatory factors that bind to receptors
424 expressed primarily on neutrophils, T cells and NK cells. Notably, the heat map in Figure 6A
425 shows that apart from immune cells, fibroblasts synthesize the majority of cytokines and
426 chemokines but not tumor cells, indicating that not the cancer cells but the stromal cells
427 (fibroblasts) are key players in immune cell recruitment and activation. Indeed, we confirmed
428 that fibroblasts treated with the secretome of skin cancer cells are capable of activating T
429 cells. Furthermore, since mCAFs ensheath tumor nests and synthesize large amounts of ECM
430 proteins, it is likely that they are involved in T cell exclusion (Figure 5E,F).
431
432 **Discussion:**
433 Fibroblasts are important contributors to the TME. They can exert pro- as well as anti-
434 tumorigenic functions by stimulating tumor cell survival and proliferation, modifying ECM
435 stiffness, supporting metastasis, influencing therapy response, regulating immune cell
436 recruitment via chemokine secretion and inflammatory responses [36,76]. Inter- and
437 intratumoral CAF heterogeneity have been appreciated ever since scRNA-seq methods have
438 become available. However, their different functions in the TME remain largely inexplicit. The
439 scRNA-seq based works that have been published for skin cancers, four melanoma studies
440 [21,23–25], one SCC study [22] and one study containing BCCs and SCCs [26], either only contained a
441 very small number of fibroblasts or fibroblast heterogeneity was not the focus of the analysis.
442 Considering the large knowledge about fibroblast diversity in healthy human dermis [10–12,39], a
443 screen on the CAF heterogeneity in human skin tumors was required to fill the missing gap,
444 which we achieved with the present work, especially since our dataset comprises the three
445 major skin cancer types, and because we validated our findings not only in other published
446 datasets but also by comprehensive spatial analysis of the different CAF subsets *in situ*.
447 We have previously shown that healthy human skin comprises two functionally distinct
448 fibroblast subsets (papillary and reticular fibroblasts) which can be distinguished by the
449 expression of *CD90* (*THY1*) [39]. The present scRNA-seq screen confirmed that *CD90*, which is
450 still frequently used as the sole fibroblast marker to isolate or visualize skin fibroblasts, is only
451 expressed by the reticular subpopulation (Figure S4C). Although the majority of CAFs express

452 *CD90* (Figure S4C), our data do not allow to conclude whether CAFs develop only from skin-
453 resident reticular fibroblasts or whether they acquire expression of *CD90* upon activation.
454 Of note, the RNA expression level of *FAP* in the scRNA-seq data does not reflect the FAP
455 protein expression on the fibroblasts entirely, as we used FAP and CD90 surface expression
456 to enrich for fibroblasts by FACS (Figure S1B and S4C).
457
458 In the skin cancer samples, we identified three distinct fibroblast populations (excluding the
459 small population of ucCAFs). Immunomodulatory CAFs (iCAFs) show a characteristic
460 expression of proinflammatory cytokines (*IL1B*, *IL6*), chemokines (CXCR2 ligands) and
461 immunomodulating molecules (*IDO1*) and thus seem to be analogue to the previously
462 described iCAFs in other cancer types (Figures 3B , 5E and 5F) [35]. Matrix CAFs (mCAFs), which
463 we identified as a separate CAF population, are not to be confused with myofibroblasts
464 described in other publications[35]. mCAFs exhibit increased matrix production but without the
465 expression of *ACTA2* and myosin light chain proteins (Figures 3B, S8A and S8B).
466 Most interestingly, our dataset suggested that iCAFs and mCAFs can likely be attributed to
467 skin cancer types with higher (iCAFs) and lower (mCAFs) metastatic potential. The only
468 exception were fibroblasts from BCC II, which were found in the iCAF cluster even though BCC
469 II is histologically not different to the other two BCC samples (Figure S3). Quantification of the
470 distinct CAF subsets was particularly challenging because of the varying nature of skin cancer.
471 Skin tumors display heterogeneous morphology both within a single tumor (i.e. superficial
472 tumor areas versus invasive front) and among distinct cancer subtypes. Thus, the biological
473 difference may not be well captured in numbers. Large-field spatial visualization of the CAF
474 subsets in tumor tissue samples showed an obvious difference in the CAF patterns from lower
475 to higher malignancy, along with a higher overall CAF density in the more aggressive variants
476 of the respective skin cancer subtypes (Figure 5C,D). *In situ* localization revealed that mCAFs
477 are present in all tumors but are detected in high density at the tumor-stroma border
478 especially in nodular BCC and well-differentiated SCC. That mCAFs also increase in number in
479 late-stage tumors (Figure 5, S6A and S7) is interesting in connection with the results of our
480 multiplex mRNA staining *in situ*. Future spatial transcriptomic analysis could reveal if the
481 mCAFs located at the tumor-stroma border have a distinct expression profile compared to
482 the mCAFs located within the stromal strands and without direct contact to tumor cells. This
483 may indicate, for example, dual functions of mCAFs or a potential conversion of tumor
484 ensheathing-CAFs towards a “more aggressive” iCAF-like phenotype both of which are an
485 exciting future route to explore.
486 iCAFs are more abundant in malignant tumors, especially in infiltrative BCC and in aggressive
487 melanomas (Figure 5B,C). Although there is a trend that poorly differentiated SCCs harbor
488 higher numbers of iCAFs compared to well-differentiated SCCs, the difference is not so clear
489 between these two cancer subtypes. Analysis of larger patient cohort with additional
490 stratification into further subtypes may be necessary to provide a clearer picture.
491

492 The *RGS5*$^{+}$ cluster contains cells from all samples, including healthy controls. According to
493 differential gene expression, the *RGS5*$^{+}$ cluster would commonly be termed as
494 myofibroblasts/myoCAFs due to the characteristic expression of *ACTA2*, *MYH11* and *COL1A1*.
495 However, the *RGS5*$^{+}$ cluster also showed a marker profile that can be attributed to pericytes
496 (*RGS5*, *PDGFRB*, *KCNJ8*, *TAGLN, MCAM*) (Figure 3B and 4A). We demonstrate by *in situ*
497 immunohistochemistry that *RGS5*$^{+}$ cells are not only found in a perivascular localization but
498 are also distributed throughout the stroma in tumor regions. In contrast, in unaffected skin,
499 *RGS5*$^{+}$ cells are restricted to a perivascular localization (Figure 4A and 4B). Thus, an exclusive
500 definition as myofibroblasts/myoCAFs or pericytes for this cluster seems to be inappropriate.
501 The impossibility to discern myofibroblasts/myoCAFs from pericytes on RNA level has been a
502 general issue, as we found very similar expression patterns of the myofibroblasts/pericytes in
503 a HNSCC dataset, once defined as myofibroblasts [19], and once defined as pericytes [71] (Figure
504 4C). It has been suggested that pericytes are able to leave the vessel wall and contribute to
505 the tumor stroma in a process called pericyte-fibroblast transition (PFT) [77]. To our knowledge,
506 PFT has not been shown in skin cancer. A recent pan-cancer scRNA-seq study suggested that
507 a small CAF subset arose from endothelial cells. However, this was concluded from
508 transcriptional data but not confirmed *in situ* [78]. Whether *RGS5*$^{+}$ CAFs originate from pericytes
509 or skin-resident fibroblasts cannot be concluded from this study. It is of higher importance
510 that *RGS5*$^{+}$*ACTA2*$^{+}$ CAFs are present in all tumor samples, which might represent a general
511 phenotype that is similar to activated fibroblasts expressing *ACTA2* in non-cancerous
512 conditions, such as wound healing [79,80]. Notably, Grout et al. recently described an
513 *MYH11*$^{+}$*αSMA*$^{+}$(*ACTA2*$^{+}$) and *COL4A1* expressing CAF subset in non-small cell lung cancer that
514 might be involved in T cell exclusion. The *RGS5*$^{+}$ CAFs in our study (which we appointed a T
515 cell-exclusion role from tumor nests) also expressed *MYH11*, *ACTA2* and *COL4A1*[72].
516 Reanalysis of published datasets from HNSSC [18] and cutaneous SCC [21] confirms the presence
517 of RGS5^{+} CAFs in both SCC types (Figure S13A and B), and revealed CAF subsets with
518 expression patterns similar to mCAFs and iCAFs in cutaneous SCC (Figure S13B, CAF1 and
519 CAF2). In HNSCC, the CAF1 subset displayed expression of both mCAF and iCAF genes (Figure
520 S13A). However, in the cutaneous SCC dataset, CAFs from one patient are overrepresented
521 (>50% of total fibroblasts; 92% of CAF1 and 70% of CAF2 subsets), which impedes to
522 deconstruct if CAF1 or CAF2 are more or less abundant in moderate and well differentiated
523 SCCs. We also confirmed the presence of all three CAF subsets in an independent melanoma
524 dataset (Figure S7C). Moreover, reanalysis of single cell transcriptomic data of 5 infiltrative
525 BCCs[27] confirmed the presence of mCAFs and a small cluster of iCAFs (Figure S13C).
526 Furthermore, the samples included a fibroblast cluster expressing signature genes of reticular
527 fibroblasts (Figure S13C). Of note, also in our dataset few cells from BCC and SCC contributed
528 to the rFIB cluster, most of them however from unaffected skin adjacent to the tumors (Figure
529 S4A). However RGS5^{+} cells were not included in their CAF population but might be part of the
530 pericyte population, which clustered separately in their first level clustering [27]. Garnier et al.
531 identified two clusters of *RGS5*+ and *TAGLN*+ pericytes in healthy skin and BCCs [53]. They
532 detected a selective expansion of *RGS5*+ pericytes and a reduction in *TAGLN*+ pericytes in BCC

533 compared to healthy skin, and described that the colocalization with vessel-like structures is
534 lost in BCC, indicating that these cells are similar to the *RGS5*+ *TAGLN*+ CAFs described in our
535 study. Furthermore, they detected four fibroblasts subsets which were designated as APOD+,
536 *SFRP2*+, *PTGDS*+, and *POSTN*+. Intriguingly, both *POSTN*+ and *PTGDS*+ CAFs were detected
537 around the tumor islands, suggesting that these CAFs correspond to the mCAFs in our study
538 as we used *COL11A1* and *PTGDS* to localize them in the tissue (Figure 5A).
539
540 CAFs share common features with fibroblastic reticular cells (FRCs) within lymph nodes, which
541 generate ECM conduits to guide the traffic of immune cells and the transit of potential
542 antigens [81]. It is established that CAFs participate in T-cell exclusion from tumor nests [82].
543 Several studies have reported reduced T cell infiltration in CAF-rich tumors compared to their
544 CAF-low counterparts [83]. mCAFs are detected at the tumor-stroma interface and ensheath
545 tumor nests, especially in nodular BCC and well differentiated SCC. As they synthesize a range
546 of ECM proteins including COL11A1, which we detected as dense fibers surrounding tumor
547 nests, we propose that mCAFs play a crucial role in T cell marginalization. Indeed, we detected
548 a negative correlation between T cell numbers present in tumor nests and the number of
549 mCAFs surrounding the tumor nests (Figure 5F). A similar function was described for a subset
550 of FAP^+ αSMA^+ lung CAFs expressing COL11A1/COL12A1 or COL4A1 in human lung cancer [72].
551 Thus, targeting mCAFs may improve the efficacy of immunotherapy in patients bearing T cell-
552 excluded tumors. Indeed, a whole tumor cell vaccine genetically modified to express FAP
553 significantly reduced cancer growth in a murine model of lung cancer and melanoma by
554 directly inhibiting CAFs and simultaneously enhancing T cell infiltration [84]. Whether the ECM
555 barrier formed by mCAFs modulates marginalization of other immune cells or inhibits or
556 promotes tumor cell invasion, remains to be explored.
557
558 The importance for immunomodulatory chemokines in cancer progression is undisputable.
559 The expression of CXCR2 ligands, *CXCL1-3* and *CXCL5-8* by melanoma cells has been shown to
560 control the immune cell composition of the TME, contribute to the ability to escape tumor
561 immune surveillance, induce angiogenesis or define the preferred sites of melanoma
562 metastases [85–88]. In the present study, receptor-ligand analysis revealed that fibroblasts are
563 the major source for cytokines and chemokines (Figure 6A,B) and not the cancer cells
564 themselves, thus highlighting the importance of fibroblasts in immune cell recruitment and
565 cancer immune surveillance.
566 Intriguingly, while *CXCL2* was expressed by fibroblasts from all skin cancer types, melanoma-
567 derived CAFs expressed high levels of *CXCL1-3, 5, 6* and *8* and *IL1B* as well as *IL6*, whereas the
568 expression of *CXCL9-11* and *13* was high in non-melanoma CAFs (Figure 5E). *LGALS9*, which
569 has been shown to interact with *CD40* on T cells thereby attenuating their expansion and
570 effector function, was strongly expressed in CAFs from BCC and SCC but not melanoma.
571 Furthermore, HLA genes were highly expressed in CAFs but not normal fibroblasts (Figure
572 S8B), suggesting a role for CAFs as antigen-presenting cells. CAF-mediated cross-presentation
573 of neo-antigens may directly suppress T cell function [89]. These findings indicate that although

574 iCAFs are present in melanoma and non-melanoma skin cancers, the expression of
575 chemokines and possibly other immunomodulating genes is tumor type-dependent. This is
576 also reflected by the differentially regulated expression of TFs in iCAFs derived from
577 melanoma and cSCCs (Figure 3C). We substantiated the presence of differential crosstalk
578 among tumor types and stages by testing the effect of conditioned media from various cancer
579 cell lines on healthy skin-derived fibroblasts. Indeed, conditioned medium from metastasis-
580 derived melanoma cell lines induced an iCAF-like phenotype and cytokine/chemokine
581 expression while conditioned medium of a primary melanoma cell line did not change the
582 cytokine/chemokine expression (Figure 6D). Surprisingly, the secretome of the subcutaneous
583 metastasis-derived cell line VM26 [75] did not induce the expression of the majority of the
584 tested cytokines and chemokines except for *CCL2*, which may be linked to different mutations.
585 However, VM26-derived conditioned medium was still capable of activating T cells, which is
586 not surprising as the cytokines not induced by VM26 shown in Figure 6D are CXCR1/2 ligands
587 that are known to recruit innate immune cells but not T cells. Interestingly, while the
588 secretome of melanoma and SCC cell lines was capable of inducing an iCAF phenotype,
589 induction of a mCAF phenotype could not be achieved *in vitro.* Thus, further investigations
590 are necessary to define which signals or culture conditions prime fibroblasts towards mCAF
591 differentiation *in vitro* and *in situ*. Likewise it remains elusive whether soluble CAF-derived
592 factors or direct cell contact are essential for T cell activation.
593
594 In addition to the fibroblast heterogeneity in skin tumors, our data highlight the tremendous
595 effect of the TME on all cells within a tumor. For example, melanocytes from BCC and SCC
596 samples (tMC), which are part of the non-neoplastic cells in these tumor types, cluster
597 separately from melanocytes that were derived from healthy skin samples (hMC) (Figure 2B
598 and S2C). This indicates that the altered gene expression profile is likely induced by the TME.
599 Further, our CNV analysis clearly shows that samples from the same tumor subtype
600 (Melanoma I – III: Acral lentiginous melanoma, ALM) and body location can greatly differ at
601 molecular level, which explains donor-specific clustering.
602
603 In summary, our work provides a cellular and molecular atlas of the three most frequent skin
604 cancer types comprising neoplastic epithelial, mesenchymal, and immune cells. We further
605 reveal and characterize three distinct CAF subsets and show that their abundance and
606 associated signaling molecules and structural proteins critically impact the TME. Therefore,
607 determining the predominant CAF subset within tumor samples may improve future
608 diagnostic strategies and thereby open new avenues for better personalized therapies.
609 Moreover, pharmacologically targeting CAFs to reduce ECM density could enhance T cell
610 trafficking into tumor nests and thus the efficacy of checkpoint inhibition therapy as well as
611 the penetration of agents that directly target cancer cells.
612

613 **Methods:**

614 **Human healthy skin and tumor samples**

615 Fresh 4 mm punch biopsies from central tumor and unaffected skin adjacent to tumors as
616 well as 10x10 cm healthy skin samples from abdominal plastic surgeries were subjected to
617 cell isolation procedure directly after surgery.
618 Healthy skin samples III-IV were cut into thin strips after removal of the fat layer. Epidermis
619 was separated from dermis by Dispase 2 (1:100, Roche #04942078001, 20mg/mL), digested
620 in PBS at 37°C for one hour before being peeled off. The epidermal sheet was minced and
621 then subjected to enzymatic digestion in Trypsin-EDTA (GIBCO #25300-054) for 20 min at 37°C
622 in a shaking water bath (Epidermal sheet protocol for enrichment of keratinocytes). Healthy
623 skin dermis and tumor samples were cut into tiny pieces and digested with Collagenase 1
624 (1:100, GIBCO #17100-017, 50mg/mL), Collagenase 2 (1:100, GIBCO #17101-015, 50mg/mL),
625 Collagenase 4 (1:100, Sigma-Aldrich #C5138, 50mg/mL), Hyaluronidase (1:100, Sigma-Aldrich
626 #H3884, 10mg/mL) and DNAseI (1:250, Sigma-Aldrich #DN25, 5 mg/mL) in DMEM/10%FCS for
627 one hour in a 37°C water bath (Protocol for enrichment of fibroblasts, keratinocytes and
628 immune cells). After enzymatic digestion, the cell suspension was filtered and washed in
629 PBS/10% FCS twice before subjecting it to FACS staining.
630 After Fc blocking (1:500, CD16/CD32 BD #553142, RRID:AB_394656), cell suspensions were
631 stained for 30 min at 4°C in the dark with CD45-BV605 (1:50, BioLegend #304042,
632 RRID:AB_2562106), ITGA6-PeCy7 (1:100, BioLegend #313622, RRID:AB_2561705), CDH1-
633 PeCy7 (1:200, BioLegend #147310, RRID:AB_2564188), FAP-APC (1:20, R&D Systems
634 #FAB3715A, RRID:AB_2884010), CD90-AF700 (1:30, BioLegend #328120, RRID:AB_2203302)
635 and CD31-FITC (1:30, BD Biosciences #563807), CD106-Pacific Blue (1:100, BD Biosciences
636 #744309, RRID:AB_2742138), CD235ab-Pacific Blue (1:1000, BioLegend #306611,
637 RRID:AB_2248153) and DAPI. ITGA6^{+}/CDH1^{+} keratinocytes, FAP^{+}/CD90^{+} fibroblasts, CD45^{+}
638 immune cells and FAP^{-}CD90^{-} double negative cells were single cell sorted directly into Smart-
639 seq2 lysis buffer in 384-well plates. After sorting, plates were stored at -80°C until they were
640 sent for sequencing to the Eukaryotic Single Cell Genomics Facility (ESCG) at SciLifeLab at the
641 Karolinska Institutet, Sweden.
642

643 **Ethical approval**

644 Written informed patient consent was obtained before tissue collection in accordance with
645 the Declaration of Helsinki. Our study was approved by the Institutional Review Board under
646 the ethical permits EK#1695/2021, EK#1783/2020 and EK#1555/2016.
647

648 **Immunohistochemistry**

649 Immunohistochemistry was performed on 4μm human FFPE sections according to standard
650 protocols. Antigen retrieval was conducted in citrate buffer, pH 6.0 and 3%BSA/PBST was used
651 for blocking. Primary antibodies against CD90 (THY1) (1:200, rabbit monoclonal [EPR3133],
652 Abcam #ab133350, RRID:AB_11155503), FAP (1:200, rabbit monoclonal [D3V8A], Cell
653 signaling #13801, RRID:AB_2798316), TAGLN (1:12.000, rabbit polyclonal, Thermo Scientific

654 #PA5-27463, RRID:AB_2544939), DES (1:2000, rabbit monoclonal [Y266], Abcam #ab32362,
655 RRID:AB_731901), CD31 (1:500, rabbit, Neomarkers, #RB10333-P1)), CD3 (1:200, rabbit,
656 Abcam #ab16669, RRID:AB_443425) and COL11A1 (1:200, rabbit polyclonal, Abcam
657 #ab64883, RRID:AB_1140613) were diluted in 1%BSA/PBST and incubated over night. A
658 biotinylated goat anti-rabbit antibody (1:200, Vector BA-1000) was used as second step and
659 incubated for 30 min at room temperature. Novocastra Streptavidin-HRP (Leica Biosystems
660 Newcastle #RE7104) and Dako AEC+ High sensitivity substrate (Dako #K3469) were used for
661 signal enhancement and development. For counter staining, hematoxylin was used.

662 **RNAScope**

663 RNAScope was conducted by using Multiplex Fluorescent Reagent Kit v2 from Advanced Cell
664 Diagnostics, ACD Bio-Techne (#323135), according to the manufacturer's protocol, with
665 probes for *COL1A1* (#401891-C2), *COL11A1* (#400741-C3), *PTGDS* (#431471-C1), *MMP1*
666 (#412641-C1), *RGS5* (#533421-C3) and *PDGFRA* (#604481-C1). For fluorescence staining, the
667 TSA dyes Fluorescein, Cy3 and Cy5 (Akoyabio) and DAPI as nuclear stain were utilized. The
668 Multiplex Fluorescent Reagent Kit v2 and the RNAscope® 4-Plex Ancillary kit were combined
669 for 4-plex stainings against CXCL2 (#425251), CXCL8 (310381-C2), IL24 (404301-C3) and
670 Col1A1 (401891-C4), or against MMP1 (#412641-C1), Col11A1 (#400741-C2), RGS5 (#533421-
671 C3) and COL1A1 (#401891-C4). Opal™ fluorophores (Opal 520 or Opal780, Opal 570, Opal 620
672 and Opal 690) were utilized in the 4-plex staining's. Images were captured by Vectra Polaris™
673 and image analysis was conducted with HALO® image analysis platform.
674

675 **Quantification of total CAFs, iCAFs and mCAFs in tumor sections**

676 To analyze and quantify the various CAF populations in tumor sections, we utilized the HALO®
677 image analysis platform. The cell types included total CAFs (COL1A1$^+$), iCAFs
678 (COL1A1$^+$MMP1$^+$), and mCAFs (COL1A1$^+$ COL11A1$^+$ MMP1$^-$), which were identified by specific
679 marker combinations. Tumor sections from nodular (n=8) and infiltrative BCC (n=9), well (n=8)
680 and poorly (n=10) differentiated SCC, as well as low (n=8) and high (n=9) grade melanoma
681 were analyzed. A minimum of five representative regions of interest (ROIs) per sample were
682 selected, excluding scarred or ulcerated areas to ensure accurate quantification. The HALO
683 v3.6.4134 software with the HighPlex FL v4.2.14 plugin was employed for image analysis, with
684 signal intensity thresholds set for each channel to differentiate positive from negative cells.
685 Representative spatial plots were generated from analyzed sections in HALO®.

686 **T cell exclusion from tumor nests**

687 BCC samples (n=15) were stained for immunohistochemistry (IHC) with antibodies against
688 CD3, followed by staining of consecutive sections using the RNAscope 4-Plex Multiplex
689 Fluorescent Reagent Kit to *COL1A1*, *MMP1*, *Col11A1* and *RGS5*. HALO® image analysis
690 platform was used to perform image analysis and quantification. Regions of interest (ROI)
691 were selected, where CD3$^+$ cells were present in the stroma surrounding the tumor nests. A
692 machine learning classifier, which was then trained to differentiate between tumor and

693 stromal tissue, was applied to the ROIs. We quantified the number of $CD3^+$ cells in the total
694 tissue area or only in the tumor nests within the ROI. The sections were then co-registered
695 with the RNAscope staining, and the numbers of CAFs (*COL1A1*$^+$ cells) and matrix CAFs
696 (*COL1A1*$^+$*COL11A1*$^+$*MMP1*$^-$*RGS5*$^-$) were quantified. The cell counts were then normalized to
697 cells/mm².
698
699 **Fibroblast activation by conditioned medium of cancer cells: transcriptomic and proteomic**
700 **analysis**
701 Normal healthy dermal fibroblasts (NHDF) and fibroblasts from a primary melanoma were
702 isolated as described above and cultured in DMEM containing 10% FBS and 50 µg/ml
703 Gentamycin in a humidified incubator at 37°C and 5% CO_2.
704 Generation of conditioned medium (CM) from cancer cell lines: Melanoma cell lines (VM08,
705 VM15, VM19, VM25, VM26)[75] were cultured in RPMI1640 (GIBCO #11875093) containing 10%
706 FBS (GIBCO #26140079), 2 mM L-glutamine (GIBCO #25030081) and 50 U/ml
707 streptomycin/penicillin (GIBCO #15070063). SCC13[74] cell line (RRID:CVCL_4029) was cultured
708 in DMEM Glutamax containing 10 % FBS, 2 mM L-glutamine (GIBCO #25030081), 50 U/ml
709 streptomycin/penicillin (GIBCO #15070063), 5µg/ml insulin and 10 µg/ml transferrin. When
710 cells reached 70-80% confluency, they were washed with PBS, and DMEM/10% FBS was
711 added. Conditioned medium (CM) was collected 48 hours later, centrifuged with 300 g for 10
712 minutes and stored at -20°C.
713 Fibroblast activation assay: NHDF and cancer cells were seeded into 6 well plates for 24 hours.
714 Then, medium of the NHDF was exchanged with CM derived from cancer cells or from NHDF
715 as a control. Cells were harvested 72 hours later. RNA was isolated with the Qiagen RNeasy
716 Mini Kit (Qiagen #74106). RevertAid H Minus First Strand cDNA Synthesis Kit (Thermo
717 Scientific #K1631) was used to prepare cDNA after a DNaseI digestion step (Thermo Scientific
718 #EN0521). Taqman 2xUniversal PCR Master Mix (Applied Biosystems #4324018) and Taqman
719 probes for GAPDH (Hs99999905), CXCL1 (Hs00236937_m1), CXCL2 (Hs00601975_m1), CXCL3
720 (Hs00171061_m1), CXCL5 (Hs01099660_g1), CXCL6 (Hs00605742_g1), CXCL8
721 (Hs00174103_m1), CCL2 (Hs00234140_m1) and IL24 (Hs01114274_m1), Lumican
722 (Hs00929860_m1), Col11A1 (Hs01097664_m1), Col4A1 (Hs00266237_m1), LOXL2
723 (Hs00158757_m1), Fibromodulin (Hs05632658_s1) and Col12A1 (Hs00189184_m1) were
724 used in the qPCR.
725 LEGENDplex Assay: For proteomic analysis cancer CM or control medium was removed from
726 fibroblasts after 72h incubation. Cells were washed in PBS and fresh DMEM/10% FCS was
727 added for 48h. Supernatants were collected, centrifuged to remove cell debris and subjected
728 to protein analysis using LEGENDplex kits (Human Essential Immune Response #740930 and
729 Human Proinflammatory Chemokine Panel #740985, BioLegend). Data analysis was done in
730 GraphPad Prism version 8.0.0 for Windows, GraphPad Software, San Diego, California USA,
731 www.graphpad.com.
732

733 **T cell activation assay**

734 Naïve T cell isolation

735 Human peripheral blood obtained from healthy individuals (with informed consent), was
736 collected in heparinized tubes and immediately processed by mixing 1:1 with PBS, then
737 layered over Ficoll-Paque™ PLUS (Cytiva). After density gradient centrifugation at 500 x g,
738 20°C, for 20 minutes, the PBMC layer was transferred, washed with PBS, and CD4+ and CD8+ T
739 cells were isolated using the human CD4+ and CD8+ T cell isolation kits (Miltenyi Biotec),
740 according to the manufacturer's protocol. The isolated CD4+ and CD8+ T cells were stained
741 with a mix of antibodies for 20 minutes at 4°C in the dark: CD4-FITC (1:400, [RPA-
742 T4], BioLegend #300501, RRID:AB_314070), CD8-PE-Cy7 (1:100, [HIT8a] BD Biosciences Cat#
743 555635, RRID:AB_395997), CD25-APC (1:100, [BC96], BioLegend Cat# 302609 (also 302610),
744 RRID:AB_314279), CD14-APC-Cy7 (1:100, [M5E2], BioLegend Cat# 301820 (also 301819),
745 RRID:AB_493695), CD45RO-PacificBlue (1:100, [UCHL1], BioLegend Cat# 304215 (also
746 304216), RRID:AB_493658), CD127-PE (1:100, [A019D5], BioLegend Cat# 351340 (also
747 351303, 351304), RRID:AB_2564136), CD16-PerCP-Cy5.5 (1:500, [3G8], (BioLegend Cat#
748 302028 (also 302027), RRID:AB_893262)). Cells were washed with PBS and resuspended in
749 RPMI1640 without phenol red (Gibco) containing a 1:1000 dilution of 7-AAD viability dye
750 (BioLegend). Naïve CD4 or CD8 T cells were sorted with the BD FACSAria™ II Cell Sorter based
751 on CD4+CD127+CD14-CD16-CD45RO-CD25- or CD8+CD127+CD14-CD16-CD45RO-CD25-. The
752 collected T cells were stained with a proliferation dye (1:500, eBioscience, V450) for 8 minutes
753 at 37°C, followed by washing with RPMI1640 media (Gibco) containing 10% FBS, 1%
754 penicillin/streptomycin (Gibco), and 2 mM L-glutamine (Gibco).

755 Experimental setup and FACS analysis

756 2000 fibroblasts/CAFs or melanoma cells were seeded into 96-well plates using DMEM or
757 RPMI1640 media (Gibco), containing 10% FBS, 1% penicillin/streptomycin (Gibco), and 2 mM
758 L-glutamine (Gibco), respectively. After 24 hours, the medium of NHDFs were replaced with
759 conditioned medium derived from either NHDFs or cancer cells. Following 72h incubation at
760 37°C, cells were washed with PBS, and 50 µL of RPMI containing 10% FBS, 1%
761 penicillin/streptomycin (Gibco), 2 mM L-glutamine and 12.5 µL/mL Immunocult CD3/CD28 T
762 cell activator (Stemcell) was added. Then 50 µL of RPMI containing 40,000 T cells at a ratio of
763 1 (CD8) to 1.5 (CD4) were added. The cells were harvested by scraping after 24h or 96h and
764 subjected to FACS analysis for the assessment of T cell proliferation (24h) and expression of
765 CD69 (24h), CD45RO (96h) and CD62L (96h) on CD4 or CD8 T cells (negative of fibroblast
766 markers CD90 and FAP). Cells were stained in PBS/10%FCS and incubated for 20 minutes at
767 4°C in the dark: CD4-FITC (1:400, [RPA-T4], BioLegend #300501, RRID:AB_314070), CD8-PE-
768 Cy7 (1:100, [HIT8a] BD Biosciences Cat# 555635, RRID:AB_395997), CD69-PE (1:100, [FN50],
769 BioLegend Cat# 985202, RRID:AB_2924641), CD90-AF647 (1:100, [5E10], BioLegend Cat#
770 328115 (also 328116), RRID:AB_893439), FAP-APC (1:100, [427819], R&D Systems Cat#
771 FAB3715A-025), CD45RO-PacificBlue (1:100, [UCHL1], BioLegend Cat# 304244 (also 304205,
772 304206), RRID:AB_2564160), CD62L- PerCP-Cy5.5 (1:100, [DREG56], Elabscience Cat# E-AB-

773 F1051A). Following incubation, cells were washed and resuspended in PBS with Fixable
774 Viability Dye eFluor™ 780 APC-Cy7 (eBioscience) for subsequent analysis using CytoFlex LX
775 Flow Cytometer (Beckman Coulter).

776 **Single cell RNA sequencing**
777 scRNA-seq was conducted by the Eukaryotic Single Cell Genomics Facility (ESCG) at SciLifeLab,
778 Sweden according to the Smart-seq2 protocol [90]. Demultiplexed reads were aligned to the
779 human genome (hg19 assembly) and the ERCC spike-in reference using STAR v2.4.2a in two-
780 pass alignment mode [91]. Uniquely aligned reads were transformed into reads per million
781 kilobase (RPKM) using rpkmforgenes() . RPKM values were summed up when several isoforms
782 of a gene were detected.
783
784 **Single cell RNA sequencing data processing**
785 Low quality cells were removed by using thresholds for RPKM-values and number of genes
786 expressed per cell. The lower threshold was referred to empty-well controls, the upper
787 threshold was set based on unusually high RPKM-values of clearly visible outliers. We
788 considered good quality when a minimum of 400 genes and RPKM-values between 150.000-
789 8.000.000 per cell was reached. Finally, 4824 cells were retained after quality control.
790 Subsequent data analysis was carried out by using R3.6.2 and the Seurat package v3 (Stuart*,
791 Butler*, et al., Cell 2019). RPKM values for each gene per cell were normalized and natural-
792 log transformed (NormalizeData: normalization.method="Log-Normalize"). The 2000 most
793 variable genes were identified (FindVariableGenes: selection.method = 'vst'), the data scaled
794 and principal component analysis (PCA) was performed. The first 20 principal components
795 1:20, resolution 0.2 and Seurat default parameters were used for UMAP generation of first-
796 level clustering. Subsequently, clusters for second-level clustering were selected based on
797 commonly known signature gene expression: Healthy keratinocytes, SCC and BCC (*KRT5*,
798 *KRT14*), melanocytes and melanoma cells (*MLANA*), immune cells (*CD45*) as well as fibroblasts
799 and vSMCs (*COL1A1*, *RERGL*).
800 Differentially expressed genes were identified by the Seurat function FindAllMarkers. For
801 generation of UMAPs, violin and bar plots, ggplot2 v3.3.2 were used.
802
803 **Copy number variations for estimation of malignancy**
804 *InferCNV* of the Trinity CTAT Project (https://github.com/broadinstitute/inferCNV) was used
805 to calculate CNVs for healthy and malignant keratinocytes and separately for melanocytes
806 and melanoma cells in comparison to stromal cells. For CreateInfercnvObject, healthy stromal
807 cells (Healthy donor cells from Fibroblast&vSMC second level clustering, which includes
808 fibroblasts, vSMCs and pericytes) were used as reference for CNV estimation. *InferCNV*
809 operations were performed by infercnv::run using min_cells_per_gene = 3, cutoff = 1,
810 cluster_by_groups = T, denoise = T, HMM = T, analysis_mode = subclusters,
811 hclust_method = ward.D2, tumor_subcluster_partition_method = random_trees. Estimation
812 of malignancy was performed as previously described [25], using a pearson correlation cutoff of

813 0.45 or 0.40 and a sum of squares (SoS) cutoff of 0.017 or 0.026 for healthy and malignant
814 keratinocytes or melanocytes and melanoma cells, resepctively. In the CNV estimation plots
815 for melanocytes and melanoma cells (Figure S3B) we highlighted melanocytes derived from
816 cluster hMC (melanocytes derived from healthy skin) and tMC (melanocytes derived from
817 SCC, BCC and melanoma adjacent from unaffected skin samplesadjacent to melanoma) where
818 most of the cells are nicely found in the lower quadrants as expected (CNV- and undefined).
819 CNV estimation based on RNA expression only detects genomic aberrations that affects larger
820 chromosomal sections. Thus, we also analyzed the expression of certain genes in
821 keratinocytes from BCC and SCC samples in comparison to healthy keratinocytes. For
822 determining neoplastic keratinocytes in BCC samples we used PTCH1 and PTCH2[55,56] (Figure
823 S2A,B).
824
825 **Trajectory analysis**
826 We used Monocle2[65] (v2.28, R4.0.0) and Monocle3[66] (v0.2.1, R3.6.2) to perform trajectory
827 analysis. For both methods, we extracted RPKM data, phenotype data, and feature data from
828 the Seurat object (second-level clustering of fibroblasts without vSMC) from which we created
829 a newCellDataSet(lowerDetectionLimit = 0.1, expressionFamily = tobit()) or a
830 new_cell_data_set() object using default parameters.
831 For Monocle2, we converted our RPKM data into mRNA counts using relative2abs() and
832 generated the NewCellDataSet(lowerDetectionLimit = 0.5, expressionFamily =
833 negbinomial.size()) object again. As quality filtering and clustering were already performed in
834 Seurat, we directly constructed single cell trajectories using all significantly (adjusted p-value
835 < 0.01) regulated DEGs (FindMarkers()) as input parameters for ordering cells. For calculating
836 pseudotime, we used healthy skin cells from controls as our starting point. Cells were plotted
837 using plot_cell_trajectory() colored by “clusters”, “category” and “pseudotime”.
838 For Monocle 3, we manually added clusters, UMAP and PCA parameters to the
839 new_cell_data_set() object and calculated the trajectory graph with learn_graph(object,
840 use_partition = F). For calculating pseudotime we used healthy skin clusters (pFIB and rFIB) as
841 root_cells and used plot_cells(color_cells_by = "pseudotime") to present the data.
842
843 **Heatmaps**
844 *ComplexHeatmap* v2.2.0 function was used to represent gene expression of single cells or
845 mean gene expression per cluster in heatmaps as z-scores.
846
847 **Receptor-Ligand Analysis**
848 For receptor-ligand pairing the previously published method developed by Simon Joost was
849 used, but with additional adjustments for run-time and parallel computing [93]. Receptor-ligand
850 interactions were analyzed between fibroblast clusters, immune cell clusters, neoplastic and
851 healthy keratinocyte and melanocyte clusters.
852 A signature gene list, containing potential ligands and receptors of each cluster, was
853 generated by the Seurat function FindMarkers() at the level of second-level clustering.

854 Potential ligand-receptor interactions were identified by querying the combined receptor-
855 ligand database from Ramilowski et al., 2015 and Cabello-Aguilar et al., 2020.
856 For each cluster pair, the number of identified receptor-ligand pairs was compared to the
857 number of pairs obtained from an equally sized randomly sampled pool of receptors and
858 ligands. This was repeated 10.000 times to test for significantly enriched interactions ($p \leq 0.05$
859 for Benjamini-Hochberg-corrected p-values). An additional prerequisite for a valid receptor-
860 ligand pairing was the presence of at least 2.5% cells of the same donor in both of the
861 potentially interacting clusters (eg. iCAFs interacting with tCD4 requires at least 2.5% cells
862 from the same donor in each of the clusters).
863 Used packages: *python* 3.7.6, *pandas* 1.0.1, *numpy* 1.18.1, *matplotlib* 3.2.2. Receptor – Ligand
864 heatmaps were generated with *seaborn* 0.11.0 using mean z-scores per donor per cluster.
865 Additionally, we verified receptor-ligand interactions with CellChat [73]. The communication
866 probability was calculated according to default parameters. We present selected receptor-
867 ligand pairs as circular plots using the function netVisual individual(source.use = c("mCAF",
868 "iCAF"), layout = chord).
869
870 **Module Score**
871 Module Scores were calculated by AddModuleScore() function from Seurat, and genes sets
872 were represented as violin plots. Individual genes of a gene set are shown in heatmaps. Genes
873 that showed absolutely no expression in any cluster were excluded from heatmaps and
874 module score calculation (chemokines: CCL4, CCL14, CXCL7; cytokines: IL9, IL31; MMPs:
875 MMP26). Statistical analysis was done by non-parametric Wilcox rank-sum test using ggplot2
876 function stat_compare_means().
877
878 **Melanoma scRNAseq Validation Dataset**
879 For the melanoma validation dataset, pre-treatment samples (n=5) were collected from stage
880 IV melanoma patients as part of a trial investigating anti-CD20 treatment in a therapeutic
881 setting (10.1038/s41467-017-00452-4). After biopsy of a lesion, single cell suspensions were
882 immediately frozen. Thawed suspensions were subjected to scRNA-seq using the Chromium
883 Single Cell Controller and Single Cell 5' Library & Gel Bead Kit v1.1 (10X Genomics, Pleasanton,
884 CA) according to the manufacturer's protocol. Sequencing was performed using the Illumina
885 NovaSeq platform and the 150bp paired-end configuration.
886 Preprocessing of the scRNA-seq data was performed using Cell Ranger version 6.1.2 (10x
887 Genomics). Expression data was processed using R (version 4.2.1) and Seurat (version 4.0.5).
888 Cells with less than 1,000 genes or more than 10% of relative mitochondrial gene counts were
889 removed. The data was processed following Seurat's scTransform workflow. Sample-specific
890 batch effects were corrected using Harmony. Clusters were identified using Seurat's
891 "FindNeighbors" and "FindClusters" functions, using the first 32 dimensions of the Harmony-
892 corrected embedding and a resolution of 1.5. Cell types were subsequently identified based on
893 canonical markers. Heatmaps and module scores were generated as described above.
894

895 **Publicly available dataset**
896 We reanalyzed the publicly available HNSCC data set (GSE103322) using R3.6.2 and the Seurat
897 package v3 [19]. As described by the authors, we regressed for the variable
898 *processedbyMaximaenzyme*. The cell annotation, which was provided in the meta data file,
899 was used to select the cells for clustering of the fibroblasts. Based on markers that were
900 described by the authors, the clusters for CAFs, myofibroblasts and intermediate fibroblasts
901 were assigned. A heatmap (ComplexHeatmap v2.2.0) was generated presenting gene
902 expression as means of z-scores per cluster using the same genes as shown in the heatmap in
903 Figure S2C of the original publication, but extended it by commonly accepted pericyte and
904 vSMC markers.
905 Additionally, we identified our marker genes for mCAFs, iCAFs, RGS5^{+} cells and healthy
906 fibroblasts in the fibroblast population of the HNSCC data set (GSE103322)[19], cutaneous
907 human SCC (GSE144240)[22] and human invasive BCC (GSE181907)[27] and represented it in
908 heatmaps showing gene expression as means of z-scores.
909 For the human cutaneous SCC (GSE144240) dataset, fibroblast cell annotation was provided
910 by the authors.
911 For the human invasive BCC data set, cell annotations for the fibroblast subclusters (FC1-FC4),
912 as described in the original paper [27] were provided by the authors upon request. As some
913 marker genes were expressed in very few cells, we used a cutoff of at least 2% of cells
914 expressing the gene in order to include it into the heatmap.
915 For reanalysis of this datasets we used R3.6.2, Seurat package v3 and *ComplexHeatmap*
916 v2.2.0.
917
918 **Data availability**
919 Raw data are available at the European Genome-Phenome Archive (EGAS50000000365) and
920 expression matrices are accessible at GEO (GSE254918).
921
922 **Funding**
923 This project was supported by funding granted to BML (Austrian Science Fund, FWF, V525-
924 B28 and P36368-B; Anniversary Fund of the Austrian National Bank, OeNB, 17855; City of
925 Vienna Fund for innovative interdisciplinary Cancer Research, AP00919OFF, 21059 and 22059;
926 LEO Foundation, LF-AW_EMEA-21-400116), to AF (Hochschuljubiläumsfond of the City of
927 Vienna H-283774/2019), to TJ (Karolinska Institutet, KID), to MK (Swedish Cancer Society, CAN
928 2018/793; Swedish Research Council, 2018-02963; LEO Foundation, LF-OC-19-000225;
929 Karolinska Institutet, 2-2111/2019), and SNW (Austrian Science Fund, FWF, P31127-B28).
930

931 **Acknowledgements**
932 We cordially thank Hao Yuan, Alexander Enz and Matthias Wielscher for assisting with
933 bioinformatic data processing, Robert Loewe and Philipp Weber for their help in sample
934 collection, Robin Ristl from the Institute of Medical Statistics for his support in statistical data

935 analysis, as well as Erwin Wagner, Reinhard Kirnbauer and Alessandra Handisurya for their
936 support and critical feedback. Special thanks to Nina Zila, Monika Weiss and Karin Neumüller
937 for their technical assistance and lab organization. We thank Andreas Spittler, Günther
938 Hofbauer as well as Marion Gröger, Sabine Rauscher and Christoph Friedl from the Flow
939 Cytometry and Imaging core facilities of the Medical University Vienna for their continuous
940 support. Finally, we thank the Eukaryotic Single Cell Genomics Facility (ESCG) at SciLifeLab,
941 Sweden for sequencing our cells and the national UPPMAX SENS computational infrastructure
942 for data transfer. Computation of *inferCNV* and *CellChat* were performed using the Vienna
943 Scientific Cluster 3 (VSC-3).

944
945

946 **REFERENCES**

947 1. Gieniec, K.A., Butler, L.M., Worthley, D.L., and Woods, S.L. (2019). Cancer-associated
948 fibroblasts—heroes or villains? Br J Cancer *121*, 293–302. https://doi.org/10.1038/s41416-
949 019-0509-3.

950 2. Kalluri, R. (2016). The biology and function of fibroblasts in cancer. Nat Rev Cancer *16*,
951 582–598. https://doi.org/10.1038/nrc.2016.73.

952 3. Li, T., Yang, Y., Hua, X., Wang, G., Liu, W., Jia, C., Tai, Y., Zhang, Q., and Chen, G. (2012).
953 Hepatocellular carcinoma-associated fibroblasts trigger NK cell dysfunction via PGE2 and IDO.
954 Cancer Letters *318*, 154–161. https://doi.org/10.1016/j.canlet.2011.12.020.

955 4. Mariathasan, S., Turley, S.J., Nickles, D., Castiglioni, A., Yuen, K., Wang, Y., Kadel III,
956 E.E., Koeppen, H., Astarita, J.L., Cubas, R., et al. (2018). TGFβ attenuates tumour response to
957 PD-L1 blockade by contributing to exclusion of T cells. Nature *554*, 544–548.
958 https://doi.org/10.1038/nature25501.

959 5. Özdemir, B.C., Pentcheva-Hoang, T., Carstens, J.L., Zheng, X., Wu, C.-C., Simpson, T.R.,
960 Laklai, H., Sugimoto, H., Kahlert, C., Novitskiy, S.V., et al. (2014). Depletion of Carcinoma-
961 Associated Fibroblasts and Fibrosis Induces Immunosuppression and Accelerates Pancreas
962 Cancer with Reduced Survival. Cancer Cell *25*, 719–734.
963 https://doi.org/10.1016/j.ccr.2014.04.005.

964 6. Paulsson, J., and Micke, P. (2014). Prognostic relevance of cancer-associated
965 fibroblasts in human cancer. Seminars in Cancer Biology *25*, 61–68.
966 https://doi.org/10.1016/j.semcancer.2014.02.006.

967 7. Rhim, A.D., Oberstein, P.E., Thomas, D.H., Mirek, E.T., Palermo, C.F., Sastra, S.A.,
968 Dekleva, E.N., Saunders, T., Becerra, C.P., Tattersall, I.W., et al. (2014). Stromal Elements Act
969 to Restrain, Rather Than Support, Pancreatic Ductal Adenocarcinoma. Cancer Cell *25*, 735–
970 747. https://doi.org/10.1016/j.ccr.2014.04.021.

971 8. Lichtenberger, B.M., and Kasper, M. (2021). Cellular heterogeneity and
972 microenvironmental control of skin cancer. J Intern Med *289*, 614–628.
973 https://doi.org/10.1111/joim.13177.

974 9. Mezawa, Y., and Orimo, A. (2021). Phenotypic heterogeneity, stability and plasticity in
975 tumor-promoting carcinoma-associated fibroblasts. FEBS J, febs.15851.
976 https://doi.org/10.1111/febs.15851.

977 10. Philippeos, C., Telerman, S.B., Oulès, B., Pisco, A.O., Shaw, T.J., Elgueta, R., Lombardi,
978 G., Driskell, R.R., Soldin, M., Lynch, M.D., et al. (2018). Spatial and Single-Cell Transcriptional
979 Profiling Identifies Functionally Distinct Human Dermal Fibroblast Subpopulations. Journal of
980 Investigative Dermatology *138*, 811–825. https://doi.org/10.1016/j.jid.2018.01.016.

981 11. Tabib, T., Morse, C., Wang, T., Chen, W., and Lafyatis, R. (2018). SFRP2/DPP4 and
982 FMO1/LSP1 Define Major Fibroblast Populations in Human Skin. Journal of Investigative
983 Dermatology *138*, 802–810. https://doi.org/10.1016/j.jid.2017.09.045.

984 12. Vorstandlechner, V., Laggner, M., Kalinina, P., Haslik, W., Radtke, C., Shaw, L.,
985 Lichtenberger, B.M., Tschachler, E., Ankersmit, H.J., and Mildner, M. (2020). Deciphering the
986 functional heterogeneity of skin fibroblasts using single-cell RNA sequencing. FASEB j. *34*,
987 3677–3692. https://doi.org/10.1096/fj.201902001RR.

988 13. Kieffer, Y., Hocine, H.R., Gentric, G., Pelon, F., Bernard, C., Bourachot, B., Lameiras, S.,
989 Albergante, L., Bonneau, C., Guyard, A., et al. (2020). Single-Cell Analysis Reveals Fibroblast
990 Clusters Linked to Immunotherapy Resistance in Cancer. Cancer Discov *10*, 1330–1351.
991 https://doi.org/10.1158/2159-8290.CD-19-1384.

992 14. Cords, L., Tietscher, S., Anzeneder, T., Langwieder, C., Rees, M., De Souza, N., and
993 Bodenmiller, B. (2023). Cancer-associated fibroblast classification in single-cell and spatial
994 proteomics data. Nat Commun *14*, 4294. https://doi.org/10.1038/s41467-023-39762-1.

995 15. Norton, J., Foster, D., Chinta, M., Titan, A., and Longaker, M. (2020). Pancreatic Cancer
996 Associated Fibroblasts (CAF): Under-Explored Target for Pancreatic Cancer Treatment.
997 Cancers *12*, 1347. https://doi.org/10.3390/cancers12051347.

998 16. Wang, Y., Liang, Y., Xu, H., Zhang, X., Mao, T., Cui, J., Yao, J., Wang, Y., Jiao, F., Xiao, X.,
999 et al. (2021). Single-cell analysis of pancreatic ductal adenocarcinoma identifies a novel
1000 fibroblast subtype associated with poor prognosis but better immunotherapy response. Cell
1001 Discov *7*, 36. https://doi.org/10.1038/s41421-021-00271-4.

1002 17. Khaliq, A.M., Kurt, Z., Grunvald, M.W., Erdogan, C., Turgut, S.S., Rand, T., Khare, S.,
1003 Borgia, J.A., Hayden, D.M., Pappas, S.G., et al. (2021). Redefining tumor classification and
1004 clinical stratification through a colorectal cancer single-cell atlas. bioRxiv, 2021.02.02.429256.
1005 https://doi.org/10.1101/2021.02.02.429256.

1006 18. Pelka, K., Hofree, M., Chen, J.H., Sarkizova, S., Pirl, J.D., Jorgji, V., Bejnood, A., Dionne,
1007 D., Ge, W.H., Xu, K.H., et al. (2021). Spatially organized multicellular immune hubs in human
1008 colorectal cancer. Cell *184*, 4734-4752.e20. https://doi.org/10.1016/j.cell.2021.08.003.

1009 19. Puram, S.V., Tirosh, I., Parikh, A.S., Patel, A.P., Yizhak, K., Gillespie, S., Rodman, C., Luo,
1010 C.L., Mroz, E.A., Emerick, K.S., et al. (2017). Single-Cell Transcriptomic Analysis of Primary and
1011 Metastatic Tumor Ecosystems in Head and Neck Cancer. Cell *171*, 1611-1624.e24.
1012 https://doi.org/10.1016/j.cell.2017.10.044.

1013 20. Guo, T., Li, W., and Cai, X. (2020). Applications of Single-Cell Omics to Dissect Tumor
1014 Microenvironment. Front. Genet. *11*, 548719. https://doi.org/10.3389/fgene.2020.548719.

1015 21. Jerby-Arnon, L., Shah, P., Cuoco, M.S., Rodman, C., Su, M.-J., Melms, J.C., Leeson, R.,
1016 Kanodia, A., Mei, S., Lin, J.-R., et al. (2018). A Cancer Cell Program Promotes T Cell Exclusion
1017 and Resistance to Checkpoint Blockade. Cell *175*, 984-997.e24.
1018 https://doi.org/10.1016/j.cell.2018.09.006.

1019 22. Ji, A.L., Rubin, A.J., Thrane, K., Jiang, S., Reynolds, D.L., Meyers, R.M., Guo, M.G.,
1020 George, B.M., Mollbrink, A., Bergenstråhle, J., et al. (2020). Multimodal Analysis of
1021 Composition and Spatial Architecture in Human Squamous Cell Carcinoma. Cell *182*, 497-
1022 514.e22. https://doi.org/10.1016/j.cell.2020.05.039.

1023 23. Li, H., van der Leun, A.M., Yofe, I., Lubling, Y., Gelbard-Solodkin, D., van Akkooi, A.C.J.,
1024 van den Braber, M., Rozeman, E.A., Haanen, J.B.A.G., Blank, C.U., et al. (2019). Dysfunctional
1025 CD8 T Cells Form a Proliferative, Dynamically Regulated Compartment within Human
1026 Melanoma. Cell *176*, 775-789.e18. https://doi.org/10.1016/j.cell.2018.11.043.

1027 24. Sade-Feldman, M., Yizhak, K., Bjorgaard, S.L., Ray, J.P., de Boer, C.G., Jenkins, R.W.,
1028 Lieb, D.J., Chen, J.H., Frederick, D.T., Barzily-Rokni, M., et al. (2018). Defining T Cell States
1029 Associated with Response to Checkpoint Immunotherapy in Melanoma. Cell *175*, 998-
1030 1013.e20. https://doi.org/10.1016/j.cell.2018.10.038.

1031 25. Tirosh, I., Izar, B., Prakadan, S.M., Wadsworth, M.H., Treacy, D., Trombetta, J.J.,
1032 Rotem, A., Rodman, C., Lian, C., Murphy, G., et al. (2016). Dissecting the multicellular
1033 ecosystem of metastatic melanoma by single-cell RNA-seq. Science *352*, 189–196.
1034 https://doi.org/10.1126/science.aad0501.

1035 26. Yost, K.E., Satpathy, A.T., Wells, D.K., Qi, Y., Wang, C., Kageyama, R., McNamara, K.L.,
1036 Granja, J.M., Sarin, K.Y., Brown, R.A., et al. (2019). Clonal replacement of tumor-specific T cells
1037 following PD-1 blockade. Nat Med *25*, 1251–1259. https://doi.org/10.1038/s41591-019-
1038 0522-3.

1039 27. Yerly, L., Pich-Bavastro, C., Di Domizio, J., Wyss, T., Tissot-Renaud, S., Cangkrama, M.,
1040 Gilliet, M., Werner, S., and Kuonen, F. (2022). Integrated multi-omics reveals cellular and
1041 molecular interactions governing the invasive niche of basal cell carcinoma. Nat Commun *13*,
1042 4897. https://doi.org/10.1038/s41467-022-32670-w.

1043 28. Gao, Y., Li, X., Zeng, C., Liu, C., Hao, Q., Li, W., Zhang, K., Zhang, W., Wang, S., Zhao, H.,
1044 et al. (2020). CD63 $^{+}$ Cancer-Associated Fibroblasts Confer Tamoxifen Resistance to Breast
1045 Cancer Cells through Exosomal miR-22. Adv. Sci. *7*, 2002518.
1046 https://doi.org/10.1002/advs.202002518.

1047 29. Ishibashi, M., Neri, S., Hashimoto, H., Miyashita, T., Yoshida, T., Nakamura, Y.,
1048 Udagawa, H., Kirita, K., Matsumoto, S., Umemura, S., et al. (2017). CD200-positive cancer
1049 associated fibroblasts augment the sensitivity of Epidermal Growth Factor Receptor
1050 mutation-positive lung adenocarcinomas to EGFR Tyrosine kinase inhibitors. Sci Rep *7*, 46662.
1051 https://doi.org/10.1038/srep46662.

1052 30. Su, S., Chen, J., Yao, H., Liu, J., Yu, S., Lao, L., Wang, M., Luo, M., Xing, Y., Chen, F., et
1053 al. (2018). CD10+GPR77+ Cancer-Associated Fibroblasts Promote Cancer Formation and
1054 Chemoresistance by Sustaining Cancer Stemness. Cell *172*, 841-856.e16.
1055 https://doi.org/10.1016/j.cell.2018.01.009.

1056 31. Chen, Z., Zhou, L., Liu, L., Hou, Y., Xiong, M., Yang, Y., Hu, J., and Chen, K. (2020). Single-
1057 cell RNA sequencing highlights the role of inflammatory cancer-associated fibroblasts in
1058 bladder urothelial carcinoma. Nat Commun *11*, 5077. https://doi.org/10.1038/s41467-020-
1059 18916-5.

1060 32. Elyada, E., Bolisetty, M., Laise, P., Flynn, W.F., Courtois, E.T., Burkhart, R.A., Teinor,
1061 J.A., Belleau, P., Biffi, G., Lucito, M.S., et al. (2019). Cross-Species Single-Cell Analysis of

1062 Pancreatic Ductal Adenocarcinoma Reveals Antigen-Presenting Cancer-Associated
1063 Fibroblasts. Cancer Discov *9*, 1102–1123. https://doi.org/10.1158/2159-8290.CD-19-0094.

1064 33. Geng, X., Chen, H., Zhao, L., Hu, J., Yang, W., Li, G., Cheng, C., Zhao, Z., Zhang, T., Li, L.,
1065 et al. (2021). Cancer-Associated Fibroblast (CAF) Heterogeneity and Targeting Therapy of CAFs
1066 in Pancreatic Cancer. Front. Cell Dev. Biol. *9*, 655152.
1067 https://doi.org/10.3389/fcell.2021.655152.

1068 34. Öhlund, D., Handly-Santana, A., Biffi, G., Elyada, E., Almeida, A.S., Ponz-Sarvise, M.,
1069 Corbo, V., Oni, T.E., Hearn, S.A., Lee, E.J., et al. (2017). Distinct populations of inflammatory
1070 fibroblasts and myofibroblasts in pancreatic cancer. Journal of Experimental Medicine *214*,
1071 579–596. https://doi.org/10.1084/jem.20162024.

1072 35. Sahai, E., Astsaturov, I., Cukierman, E., DeNardo, D.G., Egeblad, M., Evans, R.M.,
1073 Fearon, D., Greten, F.R., Hingorani, S.R., Hunter, T., et al. (2020). A framework for advancing
1074 our understanding of cancer-associated fibroblasts. Nat Rev Cancer *20*, 174–186.
1075 https://doi.org/10.1038/s41568-019-0238-1.

1076 36. Van Hove, L., and Hoste, E. (2021). Activation of Fibroblasts in Skin Cancer. Journal of
1077 Investigative Dermatology, S0022202X21022892. https://doi.org/10.1016/j.jid.2021.09.010.

1078 37. Driskell, R.R., Lichtenberger, B.M., Hoste, E., Kretzschmar, K., Simons, B.D.,
1079 Charalambous, M., Ferron, S.R., Herault, Y., Pavlovic, G., Ferguson-Smith, A.C., et al. (2013).
1080 Distinct fibroblast lineages determine dermal architecture in skin development and repair.
1081 Nature *504*, 277–281. https://doi.org/10.1038/nature12783.

1082 38. Jiang, D., Correa-Gallegos, D., Christ, S., Stefanska, A., Liu, J., Ramesh, P., Rajendran,
1083 V., De Santis, M.M., Wagner, D.E., and Rinkevich, Y. (2018). Two succeeding fibroblastic
1084 lineages drive dermal development and the transition from regeneration to scarring. Nat Cell
1085 Biol *20*, 422–431. https://doi.org/10.1038/s41556-018-0073-8.

1086 39. Korosec, A., Frech, S., Gesslbauer, B., Vierhapper, M., Radtke, C., Petzelbauer, P., and
1087 Lichtenberger, B.M. (2019). Lineage Identity and Location within the Dermis Determine the
1088 Function of Papillary and Reticular Fibroblasts in Human Skin. Journal of Investigative
1089 Dermatology *139*, 342–351. https://doi.org/10.1016/j.jid.2018.07.033.

1090 40. Rinkevich, Y., Walmsley, G.G., Hu, M.S., Maan, Z.N., Newman, A.M., Drukker, M.,
1091 Januszyk, M., Krampitz, G.W., Gurtner, G.C., Lorenz, H.P., et al. (2015). Identification and
1092 isolation of a dermal lineage with intrinsic fibrogenic potential. Science *348*, aaa2151.
1093 https://doi.org/10.1126/science.aaa2151.

1094 41. Omland, S.H., Wettergren, E.E., Mollerup, S., Asplund, M., Mourier, T., Hansen, A.J.,
1095 and Gniadecki, R. (2017). Cancer associated fibroblasts (CAFs) are activated in cutaneous basal
1096 cell carcinoma and in the peritumoural skin. BMC Cancer *17*, 675.
1097 https://doi.org/10.1186/s12885-017-3663-0.

1098 42. Papaccio, F., Kovacs, D., Bellei, B., Caputo, S., Migliano, E., Cota, C., and Picardo, M.
1099 (2021). Profiling Cancer-Associated Fibroblasts in Melanoma. IJMS *22*, 7255.
1100 https://doi.org/10.3390/ijms22147255.

1101 43. Sasaki, K., Sugai, T., Ishida, K., Osakabe, M., Amano, H., Kimura, H., Sakuraba, M.,
1102 Kashiwa, K., and Kobayashi, S. (2018). Analysis of cancer-associated fibroblasts and the
1103 epithelial-mesenchymal transition in cutaneous basal cell carcinoma, squamous cell
1104 carcinoma, and malignant melanoma. Human Pathology *79*, 1–8.
1105 https://doi.org/10.1016/j.humpath.2018.03.006.

1106 44. Stratigos, A., Garbe, C., Lebbe, C., Malvehy, J., Del Marmol, V., Pehamberger, H., Peris,
1107 K., Becker, J.C., Zalaudek, I., Saiag, P., et al. (2015). Diagnosis and treatment of invasive
1108 squamous cell carcinoma of the skin: European consensus-based interdisciplinary guideline.
1109 European Journal of Cancer *51*, 1989–2007. https://doi.org/10.1016/j.ejca.2015.06.110.

1110 45. Waldman, A., and Schmults, C. (2019). Cutaneous Squamous Cell Carcinoma.
1111 Hematology/Oncology Clinics of North America *33*, 1–12.
1112 https://doi.org/10.1016/j.hoc.2018.08.001.

1113 46. Fernández-Figueras, M.T., Malvehi, J., Tschandl, P., Rutten, A., Rongioletti, F.,
1114 Requena, L., Kittler, H., Kerl, K., Kazakov, D., Cribier, B., et al. (2022). Position paper on a
1115 simplified histopathological classification of basal cell carcinoma: results of the European
1116 Consensus Project. Journal of the European Academy of Dermatology and Venereology *36*,
1117 351–359. https://doi.org/10.1111/jdv.17849.

1118 47. Kim, D.P., Kus, K.J.B., and Ruiz, E. (2019). Basal Cell Carcinoma Review.
1119 Hematology/Oncology Clinics of North America *33*, 13–24.
1120 https://doi.org/10.1016/j.hoc.2018.09.004.

1121 48. Curti, B.D., and Faries, M.B. (2021). Recent Advances in the Treatment of Melanoma.
1122 N Engl J Med *384*, 2229–2240. https://doi.org/10.1056/NEJMra2034861.

1123 49. Davis, L.E., Shalin, S.C., and Tackett, A.J. (2019). Current state of melanoma diagnosis
1124 and treatment. Cancer Biology & Therapy *20*, 1366–1379.
1125 https://doi.org/10.1080/15384047.2019.1640032.

1126 50. Kurokawa, I., Takahashi, K., Moll, I., and Moll, R. (2011). Expression of keratins in
1127 cutaneous epithelial tumors and related disorders - distribution and clinical significance:
1128 Keratin expression in cutaneous epithelial tumors. Experimental Dermatology *20*, 217–228.
1129 https://doi.org/10.1111/j.1600-0625.2009.01006.x.

1130 51. Hutchin, M.E., Kariapper, M.S.T., Grachtchouk, M., Wang, A., Wei, L., Cummings, D.,
1131 Liu, J., Michael, L.E., Glick, A., and Dlugosz, A.A. (2005). Sustained Hedgehog signaling is
1132 required for basal cell carcinoma proliferation and survival: conditional skin tumorigenesis
1133 recapitulates the hair growth cycle. Genes Dev. *19*, 214–223.
1134 https://doi.org/10.1101/gad.1258705.

1135 52. Reynolds, G., Vegh, P., Fletcher, J., Poyner, E.F.M., Stephenson, E., Goh, I., Botting,
1136 R.A., Huang, N., Olabi, B., Dubois, A., et al. (2021). Developmental cell programs are co-opted
1137 in inflammatory skin disease. Science *371*, eaba6500.
1138 https://doi.org/10.1126/science.aba6500.

1139 53. Ganier, C., Mazin, P., Herrera-Oropeza, G., Du-Harpur, X., Blakeley, M., Gabriel, J.,
1140 Predeus, A.V., Cakir, B., Prete, M., Harun, N., et al. (2024). Multiscale spatial mapping of cell
1141 populations across anatomical sites in healthy human skin and basal cell carcinoma. Proc.
1142 Natl. Acad. Sci. U.S.A. *121*, e2313326120. https://doi.org/10.1073/pnas.2313326120.

1143 54. Alexandrov, L.B., Nik-Zainal, S., Wedge, D.C., Aparicio, S.A.J.R., Behjati, S., Biankin,
1144 A.V., Bignell, G.R., Bolli, N., Borg, A., Børresen-Dale, A.-L., et al. (2013). Signatures of
1145 mutational processes in human cancer. Nature *500*, 415–421.
1146 https://doi.org/10.1038/nature12477.

1147 55. Zhang, H., Ping, X.L., Lee, P.K., Wu, X.L., Yao, Y.J., Zhang, M.J., Silvers, D.N., Ratner, D.,
1148 Malhotra, R., Peacocke, M., et al. (2001). Role of PTCH and p53 Genes in Early-Onset Basal
1149 Cell Carcinoma. The American Journal of Pathology *158*, 381–385.
1150 https://doi.org/10.1016/S0002-9440(10)63980-6.

1151 56. Bale, A.E. (2001). The hedgehog pathway and basal cell carcinomas. Human Molecular
1152 Genetics *10*, 757–762. https://doi.org/10.1093/hmg/10.7.757.

1153 57. Dotto, G.P. (2014). Multifocal epithelial tumors and field cancerization: stroma as a
1154 primary determinant. J. Clin. Invest. *124*, 1446–1453. https://doi.org/10.1172/JCI72589.

1155 58. Shimomura, Y., Agalliu, D., Vonica, A., Luria, V., Wajid, M., Baumer, A., Belli, S.,
1156 Petukhova, L., Schinzel, A., Brivanlou, A.H., et al. (2010). APCDD1 is a novel Wnt inhibitor
1157 mutated in hereditary hypotrichosis simplex. Nature *464*, 1043–1047.
1158 https://doi.org/10.1038/nature08875.

1159 59. Janson, D.G., Saintigny, G., van Adrichem, A., Mahé, C., and El Ghalbzouri, A. (2012).
1160 Different Gene Expression Patterns in Human Papillary and Reticular Fibroblasts. Journal of
1161 Investigative Dermatology *132*, 2565–2572. https://doi.org/10.1038/jid.2012.192.

1162 60. Hinz, B. (2016). The role of myofibroblasts in wound healing. Current Research in
1163 Translational Medicine *64*, 171–177. https://doi.org/10.1016/j.retram.2016.09.003.

1164 61. Armulik, A., Genové, G., and Betsholtz, C. (2011). Pericytes: Developmental,
1165 Physiological, and Pathological Perspectives, Problems, and Promises. Developmental Cell *21*,
1166 193–215. https://doi.org/10.1016/j.devcel.2011.07.001.

1167 62. He, H., Suryawanshi, H., Morozov, P., Gay-Mimbrera, J., Del Duca, E., Kim, H.J.,
1168 Kameyama, N., Estrada, Y., Der, E., Krueger, J.G., et al. (2020). Single-cell transcriptome
1169 analysis of human skin identifies novel fibroblast subpopulation and enrichment of immune
1170 subsets in atopic dermatitis. Journal of Allergy and Clinical Immunology *145*, 1615–1628.
1171 https://doi.org/10.1016/j.jaci.2020.01.042.

1172 63. Paquet-Fifield, S., Schlüter, H., Li, A., Aitken, T., Gangatirkar, P., Blashki, D., Koelmeyer,
1173 R., Pouliot, N., Palatsides, M., Ellis, S., et al. (2009). A role for pericytes as microenvironmental
1174 regulators of human skin tissue regeneration. J. Clin. Invest., JCI38535.
1175 https://doi.org/10.1172/JCI38535.

1176 64. Crisan, M., Yap, S., Casteilla, L., Chen, C.-W., Corselli, M., Park, T.S., Andriolo, G., Sun,
1177 B., Zheng, B., Zhang, L., et al. (2008). A Perivascular Origin for Mesenchymal Stem Cells in
1178 Multiple Human Organs. Cell Stem Cell *3*, 301–313.
1179 https://doi.org/10.1016/j.stem.2008.07.003.

1180 65. Qiu, X., Mao, Q., Tang, Y., Wang, L., Chawla, R., Pliner, H.A., and Trapnell, C. (2017).
1181 Reversed graph embedding resolves complex single-cell trajectories. Nat Methods *14*, 979–
1182 982. https://doi.org/10.1038/nmeth.4402.

1183 66. Cao, J., Spielmann, M., Qiu, X., Huang, X., Ibrahim, D.M., Hill, A.J., Zhang, F., Mundlos,
1184 S., Christiansen, L., Steemers, F.J., et al. (2019). The single-cell transcriptional landscape of
1185 mammalian organogenesis. Nature *566*, 496–502. https://doi.org/10.1038/s41586-019-
1186 0969-x.

1187 67. Nurmik, M., Ullmann, P., Rodriguez, F., Haan, S., and Letellier, E. (2020). In search of
1188 definitions: Cancer-associated fibroblasts and their markers. Int. J. Cancer *146*, 895–905.
1189 https://doi.org/10.1002/ijc.32193.

1190 68. Bartoschek, M., Oskolkov, N., Bocci, M., Lövrot, J., Larsson, C., Sommarin, M., Madsen,
1191 C.D., Lindgren, D., Pekar, G., Karlsson, G., et al. (2018). Spatially and functionally distinct
1192 subclasses of breast cancer-associated fibroblasts revealed by single cell RNA sequencing. Nat
1193 Commun *9*, 5150. https://doi.org/10.1038/s41467-018-07582-3.

1194 69. Hughes, S., and Chan-Ling, T. (2004). Characterization of Smooth Muscle Cell and
1195 Pericyte Differentiation in the Rat Retina In Vivo. Invest. Ophthalmol. Vis. Sci. *45*, 2795.
1196 https://doi.org/10.1167/iovs.03-1312.

1197 70. Stapor, P.C., Sweat, R.S., Dashti, D.C., Betancourt, A.M., and Murfee, W.L. (2014).
1198 Pericyte Dynamics during Angiogenesis: New Insights from New Identities. J Vasc Res *51*, 163–
1199 174. https://doi.org/10.1159/000362276.

1200 71. Dominguez, C.X., Müller, S., Keerthivasan, S., Koeppen, H., Hung, J., Gierke, S., Breart,
1201 B., Foreman, O., Bainbridge, T.W., Castiglioni, A., et al. (2020). Single-Cell RNA Sequencing
1202 Reveals Stromal Evolution into LRRC15 $^{+}$ Myofibroblasts as a Determinant of Patient Response
1203 to Cancer Immunotherapy. Cancer Discov *10*, 232–253. https://doi.org/10.1158/2159-
1204 8290.CD-19-0644.

1205 72. Grout, J.A., Sirven, P., Leader, A.M., Maskey, S., Hector, E., Puisieux, I., Steffan, F.,
1206 Cheng, E., Tung, N., Maurin, M., et al. (2022). Spatial Positioning and Matrix Programs of
1207 Cancer-Associated Fibroblasts Promote T-cell Exclusion in Human Lung Tumors. Cancer
1208 Discovery *12*, 2606–2625. https://doi.org/10.1158/2159-8290.CD-21-1714.

1209 73. Jin, S., Guerrero-Juarez, C.F., Zhang, L., Chang, I., Ramos, R., Kuan, C.-H., Myung, P.,
1210 Plikus, M.V., and Nie, Q. (2021). Inference and analysis of cell-cell communication using
1211 CellChat. Nat Commun *12*, 1088. https://doi.org/10.1038/s41467-021-21246-9.

1212 74. Lefort, K., Mandinova, A., Ostano, P., Kolev, V., Calpini, V., Kolfschoten, I., Devgan, V.,
1213 Lieb, J., Raffoul, W., Hohl, D., et al. (2007). Notch1 is a p53 target gene involved in human

1214 keratinocyte tumor suppression through negative regulation of ROCK1/2 and MRCKα kinases.
1215 Genes Dev. *21*, 562–577. https://doi.org/10.1101/gad.1484707.

1216 75. Berger, W., Hauptmann, E., Elbling, L., Vetterlein, M., Kokoschka, E.M., and Micksche,
1217 M. (1997). Possible role of the multidrug resistance-associated protein (MRP) in
1218 chemoresistance of human melanoma cells. Int. J. Cancer *71*, 108–115.
1219 https://doi.org/10.1002/(SICI)1097-0215(19970328)71:1<108::AID-IJC18>3.0.CO;2-E.

1220 76. Ping, Q., Yan, R., Cheng, X., Wang, W., Zhong, Y., Hou, Z., Shi, Y., Wang, C., and Li, R.
1221 (2021). Cancer-associated fibroblasts: overview, progress, challenges, and directions. Cancer
1222 Gene Ther *28*, 984–999. https://doi.org/10.1038/s41417-021-00318-4.

1223 77. Hosaka, K., Yang, Y., Seki, T., Fischer, C., Dubey, O., Fredlund, E., Hartman, J., Religa,
1224 P., Morikawa, H., Ishii, Y., et al. (2016). Pericyte–fibroblast transition promotes tumor growth
1225 and metastasis. Proc Natl Acad Sci USA *113*, E5618–E5627.
1226 https://doi.org/10.1073/pnas.1608384113.

1227 78. Luo, H., Xia, X., Huang, L.-B., An, H., Cao, M., Kim, G.D., Chen, H.-N., Zhang, W.-H., Shu,
1228 Y., Kong, X., et al. (2022). Pan-cancer single-cell analysis reveals the heterogeneity and
1229 plasticity of cancer-associated fibroblasts in the tumor microenvironment. Nat Commun *13*,
1230 6619. https://doi.org/10.1038/s41467-022-34395-2.

1231 79. Foster, D.S., Jones, R.E., Ransom, R.C., Longaker, M.T., and Norton, J.A. (2018). The
1232 evolving relationship of wound healing and tumor stroma. JCI Insight *3*, e99911.
1233 https://doi.org/10.1172/jci.insight.99911.

1234 80. Otranto, M., Sarrazy, V., Bonté, F., Hinz, B., Gabbiani, G., and Desmouliere, A. (2012).
1235 The role of the myofibroblast in tumor stroma remodeling. Cell Adhesion & Migration *6*, 203–
1236 219. https://doi.org/10.4161/cam.20377.

1237 81. Brown, F.D., and Turley, S.J. (2015). Fibroblastic Reticular Cells: Organization and
1238 Regulation of the T Lymphocyte Life Cycle. The Journal of Immunology *194*, 1389–1394.
1239 https://doi.org/10.4049/jimmunol.1402520.

1240 82. Koppensteiner, L., Mathieson, L., O'Connor, R.A., and Akram, A.R. (2022). Cancer
1241 Associated Fibroblasts - An Impediment to Effective Anti-Cancer T Cell Immunity. Front.
1242 Immunol. *13*, 887380. https://doi.org/10.3389/fimmu.2022.887380.

1243 83. Ford, K., Hanley, C.J., Mellone, M., Szyndralewiez, C., Heitz, F., Wiesel, P., Wood, O.,
1244 Machado, M., Lopez, M.-A., Ganesan, A.-P., et al. (2020). NOX4 Inhibition Potentiates
1245 Immunotherapy by Overcoming Cancer-Associated Fibroblast-Mediated CD8 T-cell Exclusion
1246 from Tumors. Cancer Research *80*, 1846–1860. https://doi.org/10.1158/0008-5472.CAN-19-
1247 3158.

1248 84. Ziani, L., Chouaib, S., and Thiery, J. (2018). Alteration of the Antitumor Immune
1249 Response by Cancer-Associated Fibroblasts. Front. Immunol. *9*, 414.
1250 https://doi.org/10.3389/fimmu.2018.00414.

1251 85. Dhawan, P., and Richmond, A. (2017). Role of CXCL1 in tumorigenesis of melanoma.
1252 11.

1253 86. Forsthuber, A., Lipp, K., Andersen, L., Ebersberger, S., Graña-Castro, 'Osvaldo,
1254 Ellmeier, W., Petzelbauer, P., Lichtenberger, B.M., and Loewe, R. (2019). CXCL5 as Regulator
1255 of Neutrophil Function in Cutaneous Melanoma. Journal of Investigative Dermatology *139*,
1256 186–194. https://doi.org/10.1016/j.jid.2018.07.006.

1257 87. Payne, A.S., and Cornelius, L.A. (2002). The Role of Chemokines in Melanoma Tumor
1258 Growth and Metastasis. Journal of Investigative Dermatology *118*, 915–922.
1259 https://doi.org/10.1046/j.1523-1747.2002.01725.x.

1260 88. Soler-Cardona, A., Forsthuber, A., Lipp, K., Ebersberger, S., Heinz, M., Schossleitner,
1261 K., Buchberger, E., Gröger, M., Petzelbauer, P., Hoeller, C., et al. (2018). CXCL5 Facilitates
1262 Melanoma Cell–Neutrophil Interaction and Lymph Node Metastasis. Journal of Investigative
1263 Dermatology *138*, 1627–1635. https://doi.org/10.1016/j.jid.2018.01.035.

1264 89. Harryvan, T.J., Visser, M., de Bruin, L., Plug, L., Griffioen, L., Mulder, A., van Veelen,
1265 P.A., van der Heden van Noort, G.J., Jongsma, M.L., Meeuwsen, M.H., et al. (2022). Enhanced
1266 antigen cross-presentation in human colorectal cancer-associated fibroblasts through
1267 upregulation of the lysosomal protease cathepsin S. J Immunother Cancer *10*, e003591.
1268 https://doi.org/10.1136/jitc-2021-003591.

1269 90. Picelli, S., Björklund, Å.K., Faridani, O.R., Sagasser, S., Winberg, G., and Sandberg, R.
1270 (2013). Smart-seq2 for sensitive full-length transcriptome profiling in single cells. Nat
1271 Methods *10*, 1096–1098. https://doi.org/10.1038/nmeth.2639.

1272 91. Dobin, A., and Gingeras, T.R. (2015). Mapping RNA-seq Reads with STAR. Curr Protoc
1273 Bioinformatics *51*, 11.14.1-11.14.19. https://doi.org/10.1002/0471250953.bi1114s51.

1274 92. Ramsköld, D., Luo, S., Wang, Y.-C., Li, R., Deng, Q., Faridani, O.R., Daniels, G.A.,
1275 Khrebtukova, I., Loring, J.F., Laurent, L.C., et al. (2012). Full-length mRNA-Seq from single-cell
1276 levels of RNA and individual circulating tumor cells. Nature Biotechnology *30*, 777–782.
1277 https://doi.org/10.1038/nbt.2282.

1278 93. Joost, S., Jacob, T., Sun, X., Annusver, K., La Manno, G., Sur, I., and Kasper, M. (2018).
1279 Single-Cell Transcriptomics of Traced Epidermal and Hair Follicle Stem Cells Reveals Rapid
1280 Adaptations during Wound Healing. Cell Reports *25*, 585-597.e7.
1281 https://doi.org/10.1016/j.celrep.2018.09.059.

1282 94. Ramilowski, J.A., Goldberg, T., Harshbarger, J., Kloppmann, E., Lizio, M., Satagopam,
1283 V.P., Itoh, M., Kawaji, H., Carninci, P., Rost, B., et al. (2015). A draft network of ligand–
1284 receptor-mediated multicellular signalling in human. Nat Commun *6*, 7866.
1285 https://doi.org/10.1038/ncomms8866.

1286 95. Cabello-Aguilar, S., Alame, M., Kon-Sun-Tack, F., Fau, C., Lacroix, M., and Colinge, J.
1287 (2020). SingleCellSignalR: inference of intercellular networks from single-cell transcriptomics.
1288 Nucleic Acids Research *48*, e55–e55. https://doi.org/10.1093/nar/gkaa183.

1289 **FIGURE LEGENDS:**

1290 **Figure 1. A single cell transcriptomic atlas of human BCC, SCC, melanoma and healthy skin.**
1291 (A) Workflow of donor sample processing for Smart-seq2 scRNA-seq, data analysis and
1292 verification.
1293 (B) UMAP projection of first-level clustering of 4824 cells (left). Clusters are labelled by cell
1294 types, which were identified by commonly accepted marker genes (right).
1295 (C) Expression of top marker genes for the main cell types.
1296

1297 **Figure 2. Second-level clustering of non-mesenchymal cells and CNV analysis.**
1298 (A-B) UMAP projection of second-level clustering, violin plots of signature genes as well as bar
1299 plots showing donor sample distribution per cluster are presented for healthy and neoplastic
1300 keratinocytes and melanocytes.
1301 (C) CNV analysis (based on *inferCNV* package) of tumor samples using stromal cells as
1302 reference controls. UMAPs for healthy and neoplastic keratinocytes and melanocytes:
1303 Malignant cells with a predicted CNV alteration are highlighted in red and *PTCH1*/*PTCH2*
1304 overexpressing cells without CNVs are highlighted in orange or yellow, respectively.
1305 (D) UMAP projection of second-level clustering, violin plots of signature genes as well as bar
1306 plots showing donor sample distribution per cluster are presented for immune cells. The
1307 distribution of cytotoxic, helper and regulatory T cells are depicted in separate cut-outs.
1308 (E) Heatmap of genes that reflect the resting, activation, cytotoxic, co-stimulatory or co-
1309 inhibitors status of T cell subsets from healthy and tumor samples.
1310 KC-keratinocyte, MC-melanocyte, MEL-melanoma cells, hTcells-healthy T cells, tCD8-
1311 Cytotoxic T cells, tCD4-Helper T cells, Tregs-Regulatory T cells.
1312

1313 **Figure 3. Second-level clustering of fibroblasts and vascular smooth muscle cells (vSMCs)**
1314 **results in two heathy fibroblasts populations, four CAF subsets and one vSMC cluster.**
1315 (A) UMAP of second-level clustered fibroblasts and vSMCs. Violin plots of signature genes and
1316 bar plots showing donor sample distribution per cluster.
1317 (B) Heatmap of top ten differentially expressed genes per cluster.
1318 (C) Differentially expressed transcription factors between mCAFs and iCAFs.
1319 (D) Trajectoy analysis using Monocle2. Cells were highlighted according to clusters, category
1320 or pseudotime.
1321 (E) UMAP colored in pseudotime showing trajectory results from Monocle3
1322

1323 **Figure 4. The RGS5$^+$ cells are an inhomogeneous population of CAFs and pericytes.**
1324 (A) Feature and violin plots showing the expression of fibroblast and pericyte marker genes
1325 in the RGS5$^+$ cluster. Representative immunohistochemistry of TAGLN, DES and CD31 in
1326 different regions of the tumor (intratumoral, peritumoral).
1327 (B) Representative images of *COL1A1* (green), *RGS5* (red) and *PDGFRA* (blue) RNAScope
1328 fluorescence stainings in four different regions of FFPE tissue sections from donor sample SCC
1329 IV. DAPI nuclear stain is shown in grey. Scale bar represents 20 μm.

1330 (C) Myofibroblasts in a HNSCC dataset from Puram et al. 2017, exhibits a very similar
1331 expression pattern in comparison to the RGS5$^+$ cluster in our dataset.
1332
1333 **Figure 5. mCAFs and iCAFs are characterized by the expression of ECM and**
1334 **immunomodulatory genes, respectively.**
1335 (A,B) Representative images from (A) *COL1A1* (green), *COL11A1* (red) and *PTGDS* (blue) and
1336 (B) *COL1A1* (green) and *MMP1* (red) RNAScope fluorescence stainings to identifiy mCAFs and
1337 iCAFs respectively in FFPE tissue sections from different tumor samples. DAPI nuclear stain is
1338 shown in grey. Scale bar represents 20 μm.
1339 (C) Spatial plots highlighting the spatial distribution of total CAFs (*COL1A1*), iCAFs
1340 (*COL1A1*$^+$*MMP1*$^+$*)* and mCAFs (*COL1A1*$^+$*COL11A1*$^+$) and respective H&E stainings on
1341 consecutive sections. Dashed-lined boxes show approximate area of spatial plot in H&E
1342 staining.
1343 (D) Quantification of total CAFs (*COL1A1*$^+$), iCAFs (*COL1A1*$^+$*MMP1*$^+$), and mCAFs
1344 (*COL1A1*$^+$*COL11A1*$^+$*MMP1*$^-$) in cells per mm^2 in 52 samples of nodular (n=8) and infiltrative
1345 BCC (n=9), well (n=8) and poorly (n=10) differentiated SCC as well as low- (n=8) and high-grade
1346 (n=9) melanoma. Fibroblasts numbers of at least 5 representative ROIs from each tumor were
1347 summed-up and normalized to the tissue area to capture the whole tumor tissue. Statistical
1348 analysis by Mann Whitney test, p-value ** < 0.01, * < 0.05.
1349 (E) Representative images from *COL11A1* immunohistochemistry stainings. Scale bar
1350 represents 100 μm.
1351 (F) Image analysis of CD3$^+$cells/mm^2 in tumor nests and total CAFs/mm^2 (high-low cutoff 140
1352 cells/mm^2), mCAFs/mm^2 (high-low cutoff 40 cells/mm^2) or iCAFs/mm^2 (high-low cutoff 40
1353 cells/mm^2) in 97 ROIs from nodular and infiltrative BCCs (n=15). Linear regression analysis of
1354 log(CD3$^+$cells/mm^2) in tumor nests and log(CAFs/mm^2). Representative images of CD3
1355 immunohistochemistry and *COL1A1* (green) *COL11A1* (red) RNAScope fluorescence stainings.
1356 Statistical analysis by unpaired t-test, *p<0.05.
1357
1358 **Figure 6. Fibroblasts are an important source of chemokines in the tumor.**
1359 (A) Expression of immunomodulatory genes in iCAFs compared to healthy and neoplastic
1360 keratinocytes and melanocytes and interrogation for respective receptors in healthy and
1361 neoplastic keratinocytes and melanocytes as well as immune cells.
1362 (B) Circular plots of selected receptor-ligand pairs from CellChat analysis, showing mCAF/iCAF
1363 as source cells.
1364 (C) Representative images of RNA ISH staining with probes against *CXCL2*, *CXCL8*, *IL24* and
1365 *COL1A1* of BCC, SCC and melanoma samples.
1366 (D) *In vitro* cytokine expression of NHDF after exposure to conditioned medium from NHDFs,
1367 VM08, VM15, VM26, VM19, VM25 and SCC13 cells for 72 hours in comparison to the cytokine
1368 expression of the cancer cell lines VM08, VM15, VM19 and SCC13, and to primary melanoma-
1369 derived CAFs (pMel CAFs). Statistical analysis by One-way-ANOVA and Tukey`s post hoc test
1370 for multiple comparison on log-transformed data. Significant comparisons to NHDFs are
1371 shown; *p<0.05, **p<0.01, ***p<0.001.

1372

1373 **Figure 7. Fibroblasts activate $CD4^+$ and $CD8^+$ T cells**

1374 (A) Experimental setup of T cell assays shown in B and C.

1375 (B) Proliferation assessed by flow cytometry of CD4 or CD8 T cells upon co-culture with NHDFs
1376 pre-treated with conditioned medium from cancer cells, primary melanoma-derived CAFs
1377 (pMel CAFs) or cancer cells.

1378 (C) Upregulation of the early activation marker CD69 on CD4 or CD8 T cells after 24h of co-
1379 culture with NHDFs pre-treated with conditioned medium from cancer cells, pMel CAFs or
1380 cancer cells. Data represented as fold change of percentages of cells positive for the indicated
1381 markers normalized to NHDFs. (B,C) Statistical analysis in comparison to NHDFs or to T cells
1382 only by unpaired Student's t test; *$p<0.05$, **$p<0.01$, ***$p<0.001$.

1383 (D) Schematic summary of spatial distribution of distinct CAF subsets in human skin cancer.

Figure 1

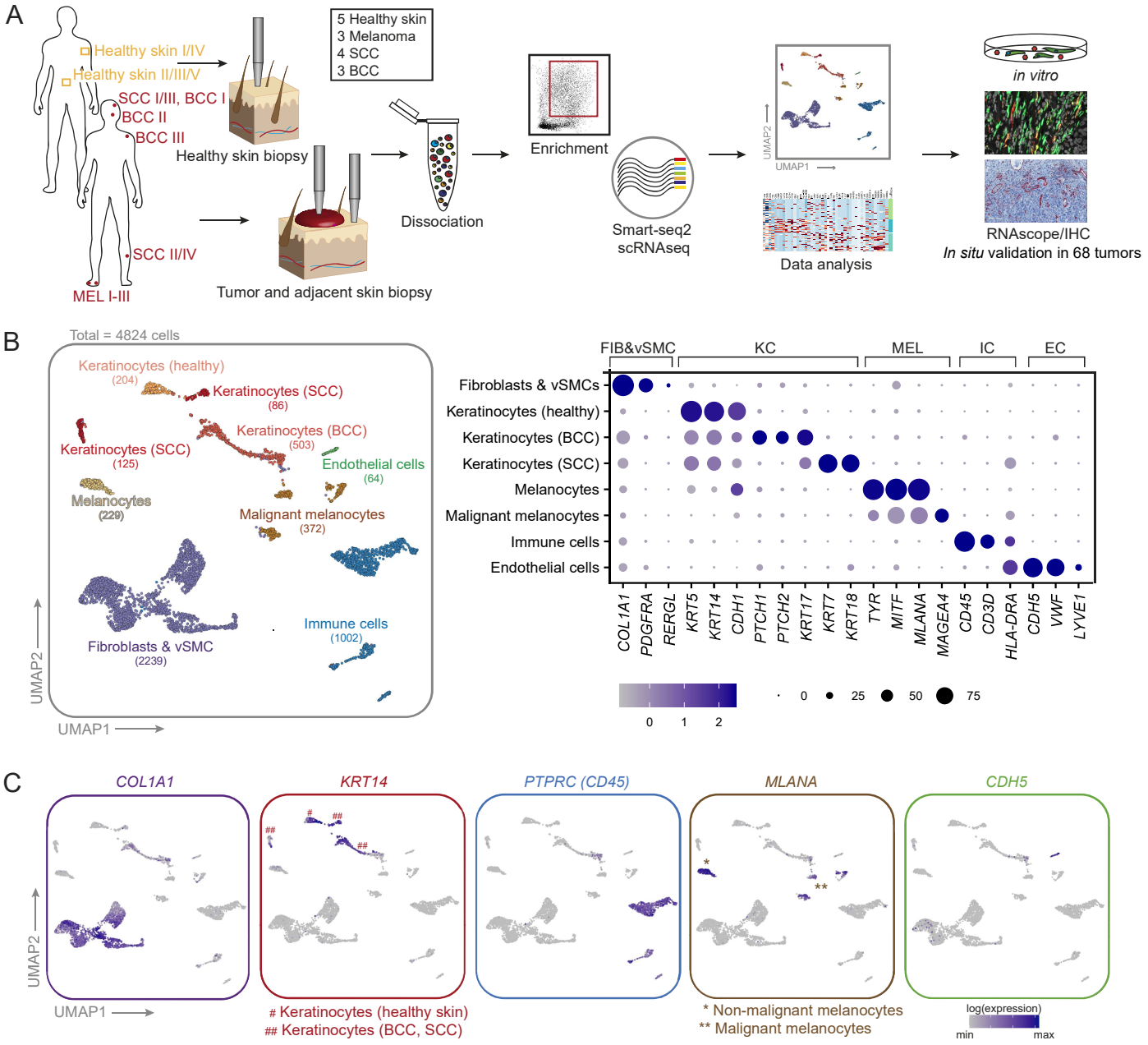
A
Healthy skin I/IV
Healthy skin II/III/V
SCC I/III, BCC I
BCC II
BCC III
SCC II/IV
MEL I-III
Healthy skin biopsy
Tumor and adjacent skin biopsy
5 Healthy skin
3 Melanoma
4 SCC
3 BCC
Dissociation
Enrichment
Smart-seq2
scRNAseq
UMAP2
UMAP1
Data analysis
in vitro
RNAscope/IHC
In situ validation in 68 tumors
B
Total = 4824 cells
Keratinocytes (healthy)
(204)
Keratinocytes (SCC)
(86)
Keratinocytes (BCC)
(503)
Keratinocytes (SCC)
(125)
Endothelial cells
(64)
Melanocytes
(229)
Malignant melanocytes
(372)
Immune cells
(1002)
Fibroblasts & vSMC
(2239)
UMAP2
UMAP1
FIB&vSMC
KC
MEL
IC
EC
Fibroblasts & vSMCs
Keratinocytes (healthy)
Keratinocytes (BCC)
Keratinocytes (SCC)
Melanocytes
Malignant melanocytes
Immune cells
Endothelial cells
COL1A1
PDGFRA
RERGL
KRT5
KRT14
CDH1
PTCH1
PTCH2
KRT17
KRT7
KRT18
TYR
MITF
MLANA
MAGEA4
CD45
CD3D
HLA-DRA
CDH5
VWF
LYVE1
0
1
2
0
25
50
75
C
COL1A1
KRT14
PTPRC (CD45)
MLANA
CDH5
UMAP2
UMAP1
Keratinocytes (healthy skin)
Keratinocytes (BCC, SCC)
* Non-malignant melanocytes
** Malignant melanocytes
log(expression)
min
max

Figure 2

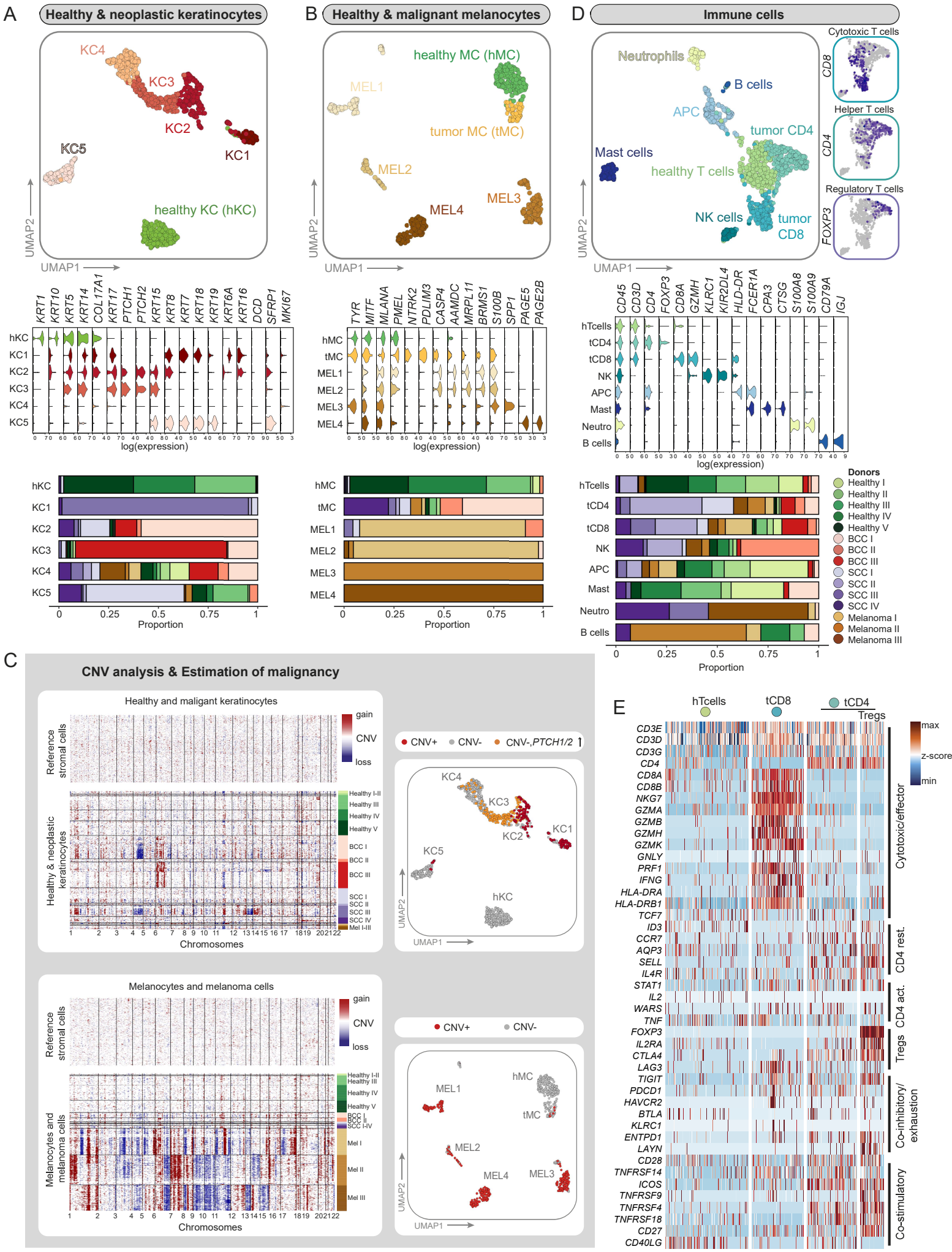
A
Healthy & neoplastic keratinocytes
KC4
KC3
KC2
KC1
KC5
healthy KC (hKC)
UMAP2
UMAP1
KRT1 KRT10 KRT5 KRT14 COL17A1 KRT17 PTCH1 PTCH2 KRT15 KRT8 KRT7 KRT18 KRT19 KRT6A KRT16 DCD SFRP1 MKI67
hKC KC1 KC2 KC3 KC4 KC5
log(expression)
hKC KC1 KC2 KC3 KC4 KC5
0 0.25 0.5 0.75 1
Proportion
B
Healthy & malignant melanocytes
healthy MC (hMC)
MEL1
tumor MC (tMC)
MEL2
MEL3
MEL4
UMAP2
UMAP1
TYR MITF MLANA PMEL NTRK2 PDLIM3 CASP4 AAMDC MRPL11 BRMS1 S100B SPP1 PAGE5 PAGE2B
hMC tMC MEL1 MEL2 MEL3 MEL4
log(expression)
hMC tMC MEL1 MEL2 MEL3 MEL4
0 0.25 0.5 0.75 1
Proportion
D
Immune cells
Neutrophils
B cells
APC
tumor CD4
Mast cells
healthy T cells
NK cells
tumor CD8
UMAP2
UMAP1
Cytotoxic T cells
CD8
Helper T cells
CD4
Regulatory T cells
FOXP3
CD45 CD3D CD4 FOXP3 CD8A GZMH KLRC1 KIR2DL4 HLD-DR FCER1A CPA3 CTSG S100A8 S100A9 CD79A IGJ
hTcells tCD4 tCD8 NK APC Mast Neutro B cells
log(expression)
hTcells tCD4 tCD8 NK APC Mast Neutro B cells
0 0.25 0.5 0.75 1
Proportion
Donors
Healthy I
Healthy II
Healthy III
Healthy IV
Healthy V
BCC I
BCC II
BCC III
SCC I
SCC II
SCC III
SCC IV
Melanoma I
Melanoma II
Melanoma III
C
CNV analysis & Estimation of malignancy
Healthy and maligant keratinocytes
Reference stromal cells
Healthy & neoplastic keratinocytes
gain
CNV
loss
Healthy I-II
Healthy III
Healthy IV
Healthy V
BCC I
BCC II
BCC III
SCC I
SCC II
SCC III
SCC IV
Mel I-III
Chromosomes
CNV+ CNV- CNV-,PTCH1/2
KC4 KC3 KC2 KC1 KC5 hKC
UMAP2
UMAP1
Melanocytes and melanoma cells
Reference stromal cells
Melanocytes and melanoma cells
gain
CNV
loss
Healthy I-II
Healthy III
Healthy IV
Healthy V
BCC I
BCC II
SCC I-IV
Mel I
Mel II
Mel III
Chromosomes
CNV+ CNV-
MEL1 hMC tMC MEL2 MEL4 MEL3
UMAP2
UMAP1
E
hTcells
tCD8
tCD4
Tregs
max
z-score
min
CD3E CD3D CD3G CD4 CD8A CD8B NKG7 GZMA GZMB GZMH GZMK GNLY PRF1 IFNG HLA-DRA HLA-DRB1 TCF7
Cytotoxic/effector
ID3 CCR7 AQP3 SELL IL4R
CD4 rest.
STAT1 IL2 WARS TNF
CD4 act.
FOXP3 IL2RA CTLA4 LAG3
Tregs
TIGIT PDCD1 HAVCR2 BTLA KLRC1 ENTPD1 LAYN
Co-inhibitory/ exhaustion
CD28 TNFRSF14 ICOS TNFRSF9 TNFRSF4 TNFRSF18 CD27 CD40LG
Co-stimulatory

Figure 3

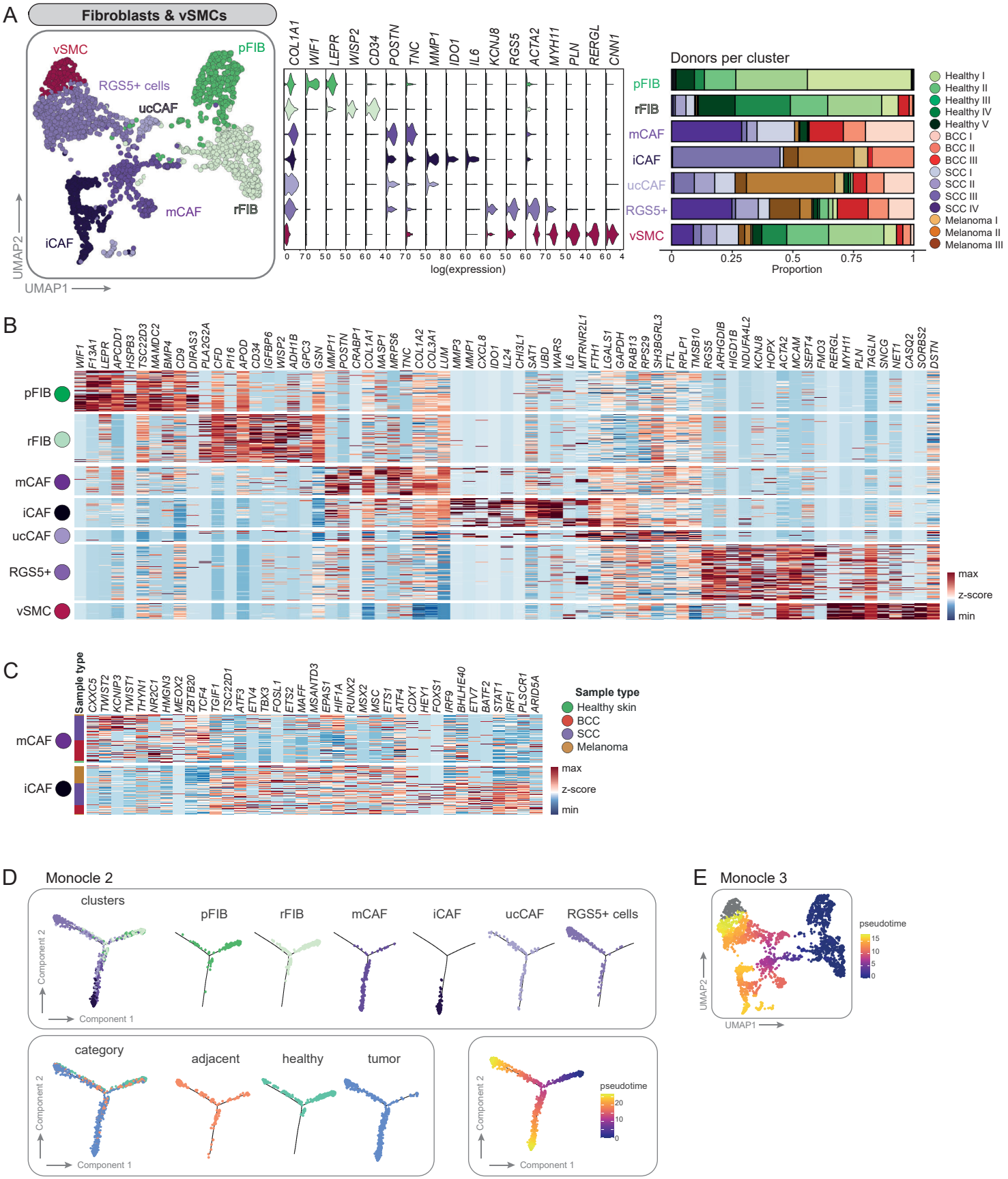
A
Fibroblasts & vSMCs
vSMC
pFIB
RGS5+ cells
ucCAF
mCAF
rFIB
iCAF
UMAP2
UMAP1
COL1A1
WIF1
LEPR
WISP2
CD34
POSTN
TNC
MMP1
IDO1
IL6
KCNJ8
RGS5
ACTA2
MYH11
PLN
RERGL
CNN1
log(expression)
Donors per cluster
Proportion
Healthy I
Healthy II
Healthy III
Healthy IV
Healthy V
BCC I
BCC II
BCC III
SCC I
SCC II
SCC III
SCC IV
Melanoma I
Melanoma II
Melanoma III
B
max
z-score
min
C
Sample type
Healthy skin
BCC
SCC
Melanoma
D
Monocle 2
clusters
category
adjacent
healthy
tumor
pseudotime
Component 1
Component 2
E
Monocle 3
pseudotime
UMAP2
UMAP1

Figure 4

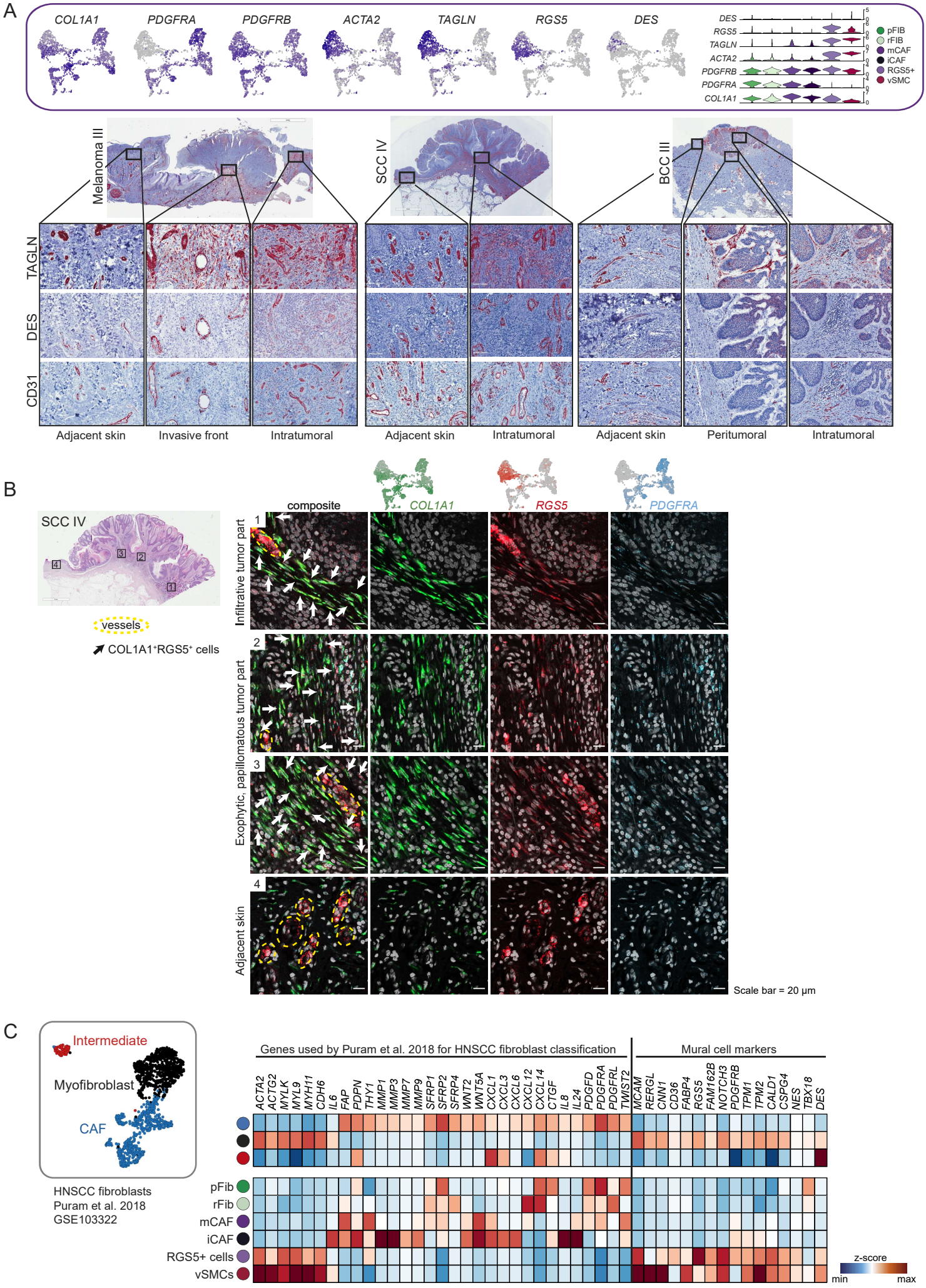
A
COL1A1
PDGFRA
PDGFRB
ACTA2
TAGLN
RGS5
DES
pFIB
rFIB
mCAF
iCAF
RGS5+
vSMC
Melanoma III
SCC IV
BCC III
TAGLN
DES
CD31
Adjacent skin
Invasive front
Intratumoral
Adjacent skin
Intratumoral
Adjacent skin
Peritumoral
Intratumoral
B
SCC IV
vessels
COL1A1+RGS5+ cells
composite
COL1A1
RGS5
PDGFRA
Infiltrative tumor part
Exophytic, papillomatous tumor part
Adjacent skin
Scale bar = 20 µm
C
Intermediate
Myofibroblast
CAF
HNSCC fibroblasts
Puram et al. 2018
GSE103322
Genes used by Puram et al. 2018 for HNSCC fibroblast classification
Mural cell markers
ACTA2 ACTG2 MYLK MYL9 MYH11 CDH6 IL6 FAP PDPN THY1 MMP1 MMP3 MMP7 MMP9 SFRP1 SFRP2 SFRP4 WNT2 WNT5A CXCL1 CXCL3 CXCL6 CXCL12 CXCL14 CTGF IL8 IL24 PDGFD PDGFRA PDGFRL TWIST2
MCAM RERGL CNN1 CD36 FABP4 RGS5 FAM162B NOTCH3 PDGFRB TPM1 TPM2 CALD1 CSPG4 NES TBX18 DES
pFib
rFib
mCAF
iCAF
RGS5+ cells
vSMCs
z-score
min
max

Figure 5

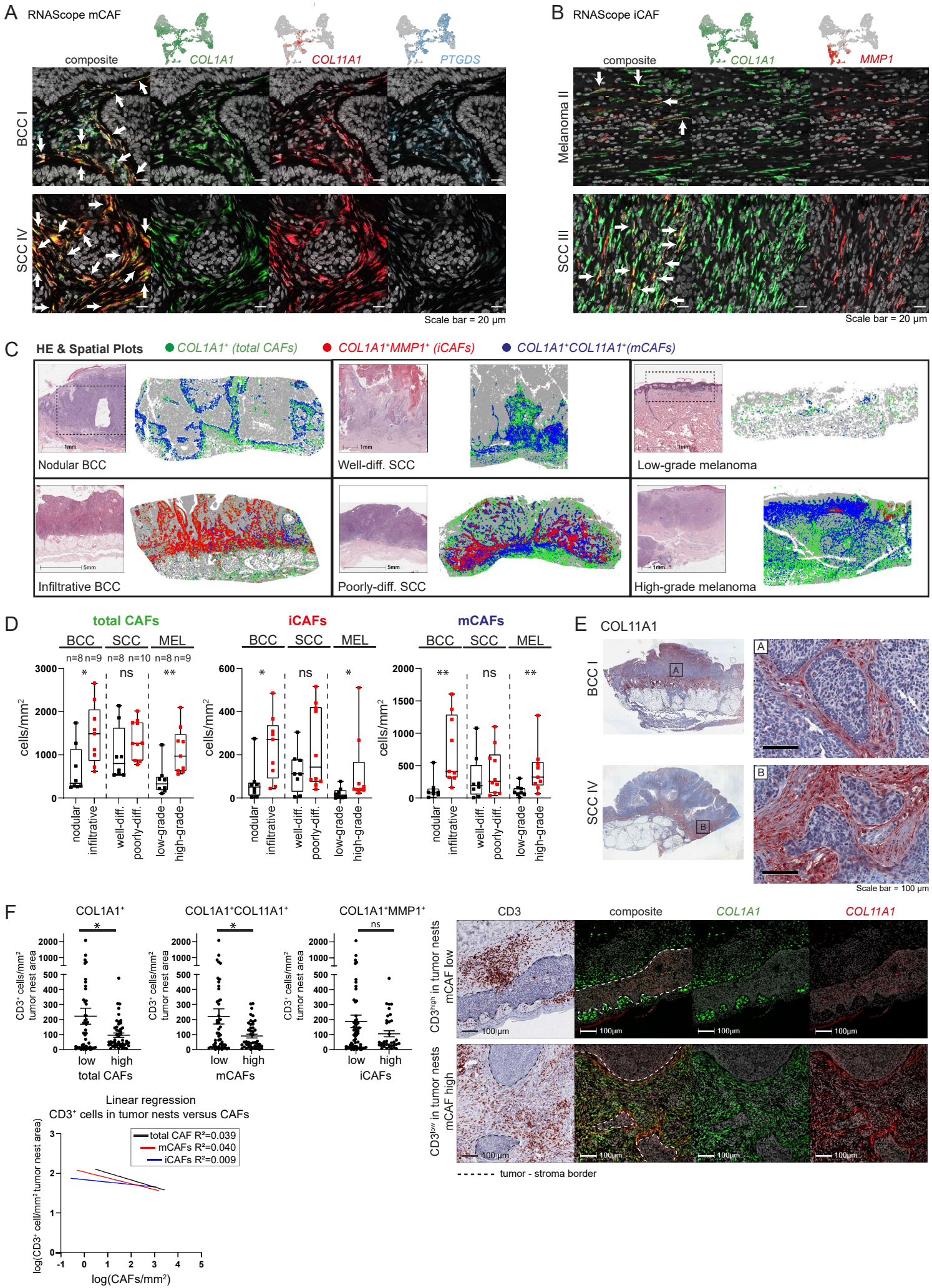
A RNAScope mCAF
composite
COL1A1
COL11A1
PTGDS
BCC I
SCC IV
Scale bar = 20 µm
B RNAScope iCAF
composite
COL1A1
MMP1
Melanoma II
SCC III
Scale bar = 20 µm
C HE & Spatial Plots
COL1A1+ (total CAFs)
COL1A1+MMP1+ (iCAFs)
COL1A1+COL11A1+(mCAFs)
Nodular BCC
Well-diff. SCC
Low-grade melanoma
Infiltrative BCC
Poorly-diff. SCC
High-grade melanoma
D
total CAFs
iCAFs
mCAFs
BCC SCC MEL
n=8 n=9 n=8 n=10 n=8 n=9
cells/mm2
nodular
infiltrative
well-diff.
poorly-diff.
low-grade
high-grade
E COL11A1
BCC I
SCC IV
Scale bar = 100 µm
F
COL1A1+
COL1A1+COL11A1+
COL1A1+MMP1+
CD3+ cells/mm2 tumor nest area
low high
total CAFs
mCAFs
iCAFs
Linear regression
CD3+ cells in tumor nests versus CAFs
total CAF R²=0.039
mCAFs R²=0.040
iCAFs R²=0.009
log(CD3+ cell/mm2 tumor nest area)
log(CAFs/mm2)
CD3
composite
COL1A1
COL11A1
CD3high in tumor nests mCAF low
CD3low in tumor nests mCAF high
100 µm
tumor - stroma border

Figure 6

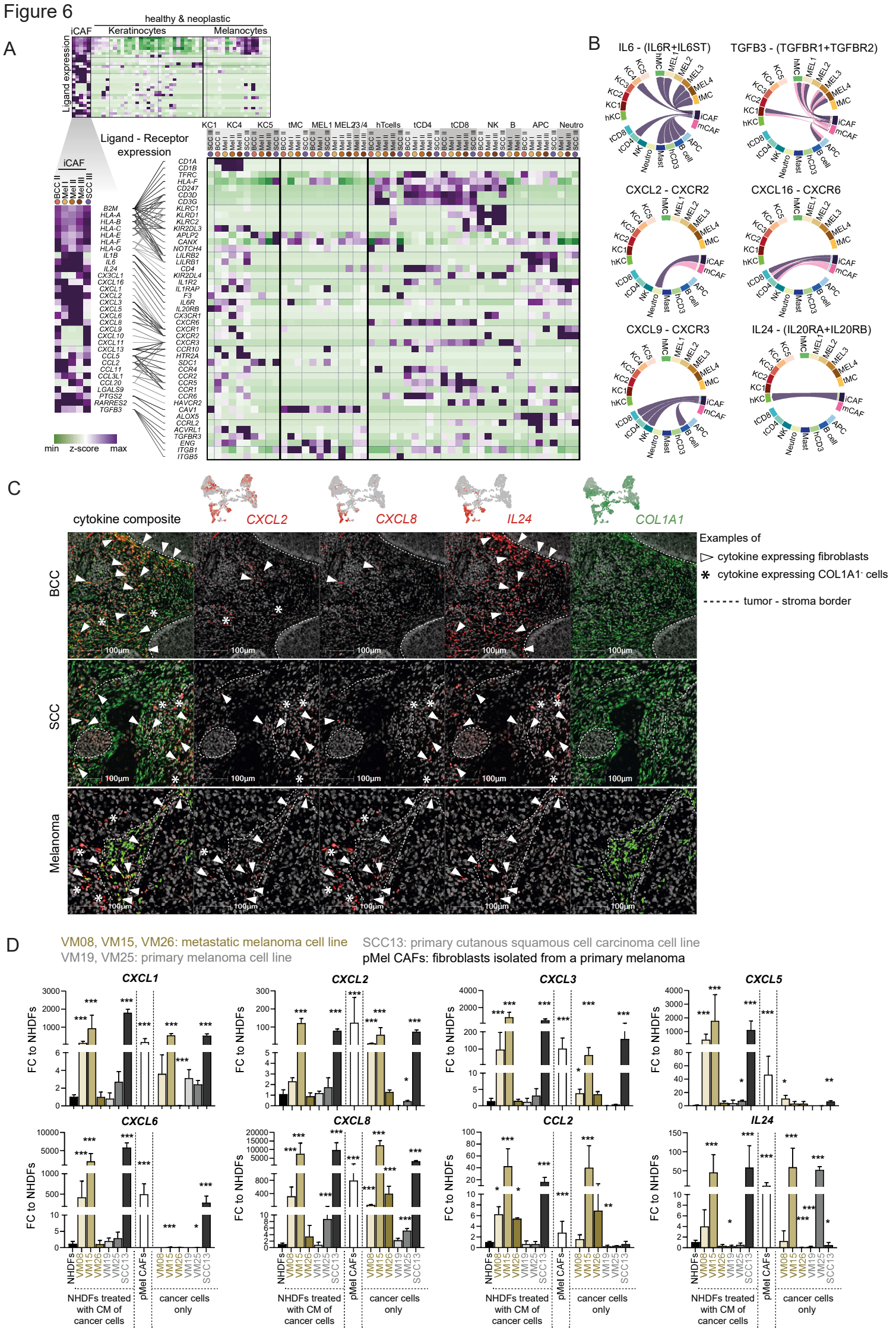
A
healthy & neoplastic
iCAF
Keratinocytes
Melanocytes
Ligand expression
Ligand - Receptor expression
KC1 KC4 KC5 tMC MEL1 MEL2/3/4 hTcells tCD4 tCD8 NK B APC Neutro
min z-score max
B
IL6 - (IL6R+IL6ST)
TGFB3 - (TGFBR1+TGFBR2)
CXCL2 - CXCR2
CXCL16 - CXCR6
CXCL9 - CXCR3
IL24 - (IL20RA+IL20RB)
C
cytokine composite
CXCL2
CXCL8
IL24
COL1A1
BCC
SCC
Melanoma
100µm
Examples of
cytokine expressing fibroblasts
cytokine expressing COL1A1- cells
tumor - stroma border
D
VM08, VM15, VM26: metastatic melanoma cell line
VM19, VM25: primary melanoma cell line
SCC13: primary cutanous squamous cell carcinoma cell line
pMel CAFs: fibroblasts isolated from a primary melanoma
CXCL1
CXCL2
CXCL3
CXCL5
CXCL6
CXCL8
CCL2
IL24
FC to NHDFs
NHDFs
VM08
VM15
VM26
VM19
VM25
SCC13
pMel CAFs
NHDFs treated with CM of cancer cells
cancer cells only

Figure 7

A

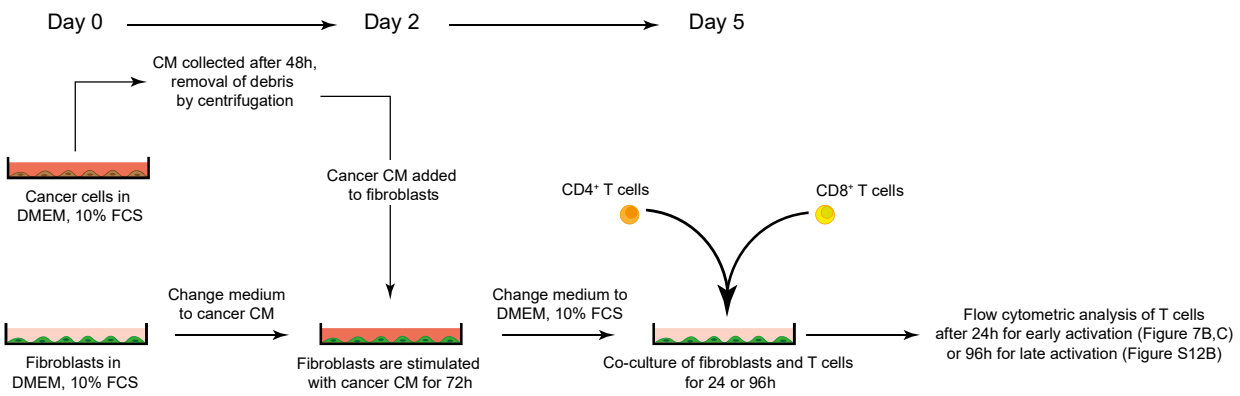

B

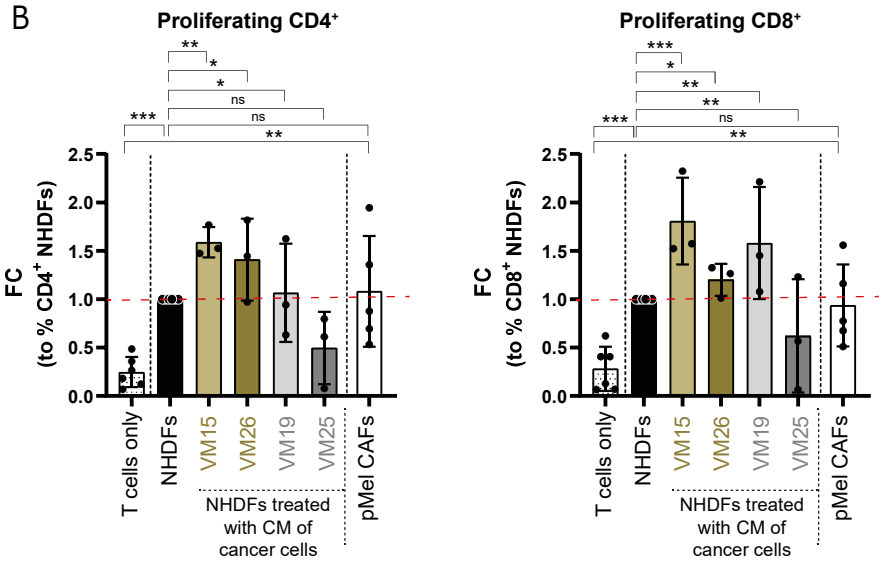

C

CD4 and CD8 T cell early activation after co-culture with CM pretreated NHDFs or primary Melanoma (pMel) CAFs

24h - early activation

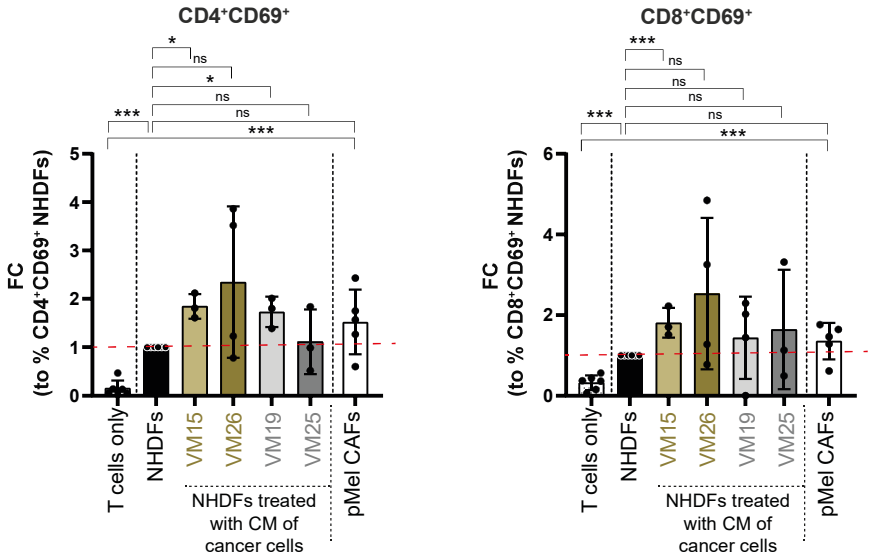

D

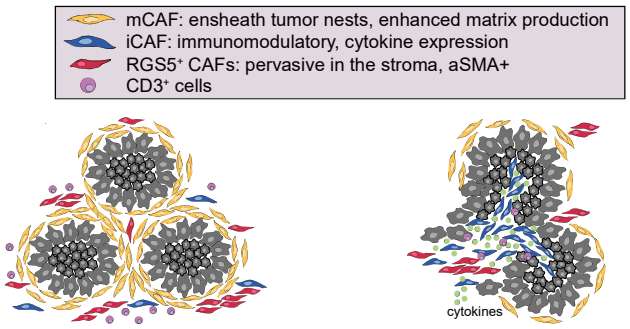

mCAFs ensheath tumor cell nests preventing T cell infiltration

Numbers of iCAFs are increased in infiltrative BCC, poorly differentiated SCC and high-grade melanoma